Chapter 3
Symmetries in Multiband Hamiltonians for Semiconductor Quantum Dots

Stanko Tomić and Nenad Vukmirović

Abstract Our current understanding of the symmetries of multiband envelope function Hamiltonians for semiconductor quantum dots and their signatures in the energy level structure and wave function shapes is reviewed. We show how symmetry can be used to block-diagonalize the Hamiltonian matrix and consequently strongly reduce the computational effort. A detailed analysis of symmetries of several different model Hamiltonians reveals that the true symmetry of square-based pyramidal quantum dots is captured if either the interface effects are taken into account or additional higher energy bands are included in the multiband Hamiltonian. This indicates that multiband envelope function methods are fully capable of capturing the true atomistic symmetry of quantum dots in contrast to some widespread beliefs. In addition, we show that translational symmetry can be artificially introduced by the numerical method used, such as the plane wave method. Plane wave method introduces artificial quantum dot replica whose charges interact with charges in the real quantum dot and create an additional strain field in the real dot. This issue can be circumvented by the introduction of proper corrections in the procedure for calculation of Coulomb integrals and strain.

S. Tomić (✉)
Joule Physics Laboratory, School of Computing, Science and Engineering,
University of Salford, Manchester M5 4WT, UK
e-mail: s.tomic@salford.ac.uk

N. Vukmirović
Scientific Computing Laboratory, Institute of Physics Belgrade, University of Belgrade,
Pregrevica 118, 11080 Belgrade, Serbia
e-mail: nenad.vukmirovic@ipb.ac.rs

M. Ehrhardt and T. Koprucki (eds.), *Multi-Band Effective Mass Approximations*,
Lecture Notes in Computational Science and Engineering 94,
DOI 10.1007/978-3-319-01427-2_3,

3.1 Introduction

Quantum dots are nanostructures which provide confinement of carriers in all three spatial directions. On the fundamental side, they enable studies of interactions between electrons and photons at the single or few particle level [1,45,61,71,74,99]. Practical applications of semiconductor quantum dots include lasers [31], optical amplifiers [8], single photon sources [45,71], photodetectors [42,50,51], fluorescent biological labels [2] and solar cells [6, 11, 28, 48, 49, 67, 72].

For these reasons, there is a tremendous need to develop both accurate and computationally efficient methods for the description of electronic states in quantum dots. In other nanostructures, such as quantum wells or wires, one can exploit the translational symmetry of the structure and consequently strongly reduce the computational cost. Single quantum dots, where no translational symmetry of the structure is present, are therefore most challenging structures for numerical studies. Nevertheless, in most cases quantum dots exhibit certain symmetry which can be exploited to reduce the computational cost. The main goal of this article is to provide understanding when and how symmetry can be exploited in numerical calculations of electronic states in quantum dots.

On the other hand, we also show that the numerical method used can introduce an artificial symmetry. This is the case for the plane wave method that assumes periodic boundary conditions which introduce an artificial translational symmetry. While such method is very useful of one wants to study the quantum dot supercrystals or quantum dot arrays [3, 34, 39, 80, 82], it needs to be modified for its applications to single quantum dot structures. In such cases, one would naturally like to remove the effects of such artefacts from the results. We show how this can be done in Sect. 3.8.

The multiband **k·p** Hamiltonians [12, 14, 15, 23, 27, 33, 44, 53, 54, 59, 60, 62–64, 68, 86, 98] are capable of reproducing the bulk bandstructure more accurately than the standard 8-band Hamiltonian. Some of these, that include a large number of bands ($\gtrsim$ 15 or 30 after incorporation of the spin degeneracies), are even capable of reproducing the bulk bandstructure throughout the whole Brillouin zone. Unfortunately, these Hamiltonians have been rarely applied to nanostructures and have not been applied to QDs at all. The effect of interface band mixing [17, 21, 32, 65, 96] has also so far been analyzed only for a single interface or a quantum well structure. The goal of this work is to explore the effects of higher bands and interfaces on the electronic structure of QDs.

In this work, we focus on self-assembled quantum dots that can be produced using epitaxial techniques [9, 52]. These typically have lateral dimensions of the order of 15–30 nm and the height of the order 3–7 nm. While ab initio calculations based on density functional theory have been performed for the clusters and nanocrystals of the size up to $\sim$3 nm [18, 25, 58, 85, 97], much larger self-assembled quantum dots are still out of the range of present day computational resources. These methods also suffer from unreliability in predicting the energy gaps. Several methods that retain the atomistic details of the system, but do not involve a self-consistent calculation,

have therefore been developed and applied to self-assembled quantum dots, such as the empirical pseudopotential method [30,93–95], the tight-binding method [35,69, 70,73], and the charge patching method [36–38,90–92].

These methods directly take into account the atomistic details of the system. This leads to their high accuracy and reliability, which is however also accompanied by a significant computational cost. In the envelope function methods (better known as the **k**·**p** method), central quantities are the slowly varying envelope functions which modulate the rapidly varying atomistic wave function. The fact that the envelope functions are slowly varying implies that less memory is needed for their representation and consequently less time is needed for their computation. This makes the method very computationally efficient and therefore attractive for the applications. We will show in this chapter that this doesn't necessary causes the lost in accuracy. We will describe the procedures for improving the envelope methods in order to reach the same level of sophistication in terms of predicting the correct symmetries of states in quantum dots as in more computationally demanding atomistic methods.

3.2 Multiband Envelope Function Method

In this section, we show how one can derive the equations that envelope functions satisfy. To simplify the derivation, we do not consider the effects of strain, piezoelectricity and spin-orbit interaction. These effects have been treated on various occasions and are well documented in the literature. Instead, we focus on the effect that is less well known—the effect of interfaces.

The single-particle Hamiltonian of an electron in a semiconductor is given as

$$H = \frac{\mathbf{p}^2}{2m_0} + V_0(\mathbf{r}), \tag{3.1}$$

where $\mathbf{p}$ is the electron momentum operator, m_0 the free electron mass and $V_0(\mathbf{r})$ the crystal potential experienced by an electron. One can think of V_0 as the self-consistent potential obtained from density functional theory or as the empirical pseudopotential. The envelope representation of the electronic wave function is given as

$$\Psi(\mathbf{r}) = \sum_i \psi_i(\mathbf{r}) u_i(\mathbf{r}), \tag{3.2}$$

where the functions $u_i(\mathbf{r})$ are orthonormal and have the periodicity of the Bravais lattice, while $\psi_i(\mathbf{r})$ are slowly varying envelope functions. The most widely used choice of the functions u_i are bulk Bloch functions at the Γ point. However, there is some ambiguity in the previous statement. If we consider a quantum dot of material A embedded in material B, are u_i the Bloch functions of material A or material B?

In what follows, we will consider that u_i are Bloch functions of some effective material C which is in some sense the average of materials A and B. For example, if materials A and B are described by pseudopotentials V_A and V_B, we will assume that the pseudopotential of the average material C is $V_C = (V_A + V_B)/2$.

After the replacement of Eq. (3.2) into the eigenvalue problem of the Hamiltonian given by Eq. (3.1) and making an approximation that eliminates the non-local terms that appear in the derivation, one arrives at the system of equations for the envelope functions [13, 22]

$$-\frac{\hbar^2}{2m_0}\nabla^2\psi_m(\mathbf{r}) + \sum_n \frac{-i\hbar}{m_0}\mathbf{p}_{mn}\cdot\nabla\psi_n(\mathbf{r}) + \sum_n H_{mn}(\mathbf{r})\psi_n(\mathbf{r}) = E\psi_m(\mathbf{r}). \quad (3.3)$$

The terms in Eq. (3.3) are defined as

$$\mathbf{p}_{mn} = \frac{1}{\Omega}\int u_m(\mathbf{r}')^*\mathbf{p}u_n(\mathbf{r}')\mathrm{d}^3\mathbf{r}', \quad (3.4)$$

where the integration goes over the volume of the crystal unit cell Ω, and

$$H_{mn} = \frac{1}{\Omega}\int u_m(\mathbf{r}')^* H u_n(\mathbf{r}')\mathrm{d}^3\mathbf{r}'. \quad (3.5)$$

Eq. (3.3) can be recast into the form

$$\sum_n h_{mn}(\mathbf{R})\psi_n(\mathbf{R}) = E\psi_m(\mathbf{R}), \quad (3.6)$$

where

$$h_{mn}(\mathbf{R}) = \frac{\hbar^2k^2}{2m_0}\delta_{mn} + \frac{\hbar}{m_0}\mathbf{k}\cdot\mathbf{p}_{mn} + [u_m|H|u_n]_{\mathbf{R}} \quad (3.7)$$

and $\mathbf{k} = -i\nabla$, while the square brackets denote the averaging over a unit cell centered at $\mathbf{R}$. The term $[u_m|V|u_n]_{\mathbf{R}}$ in the Hamiltonian [Eq. (3.7)] is a constant of a given material when $\mathbf{R}$ is far away from the interface—when the averaging does not include the interface region. Since the second term in Eq. (3.7) is crucial in the Hamiltonian matrix, the envelope function method is most frequently called the $\mathbf{k}\cdot\mathbf{p}$ method. The h_{mn} operator in Eq. (3.7) is referred to as the envelope Hamiltonian or the $\mathbf{k}\cdot\mathbf{p}$ Hamiltonian.

In practical calculations, one has to restrict to a finite number of bands in the representation in Eq. (3.2). Historically, the $\mathbf{k}\cdot\mathbf{p}$ method was first applied to valence band (6-band Hamiltonian) [40, 41] and later on the conduction band was added (8-band Hamiltonian) [55]. Recently, we have applied the 14-band and 16-band Hamiltonians (that also include the effects of strain, spin-orbit interaction, crystal field splitting and remote bands) to quantum dot structures [83]. However, these

Hamiltonians consider the last term in Eq. (3.7) as a constant of a given material and do not take into account its behavior at the interface of two materials. We will show that this term is important if one wants to understand the symmetry of the envelope function Hamiltonian and therefore devote the next section to the analysis of this term.

3.3 The Effect of Interfaces

We define the "length" of the interface L_{if} as the length of the region of space that consists of all $\mathbf{R}$-vectors such that the average $[u_m|V|u_n]_{\mathbf{R}}$ encompasses the interface region. For example, in the case of the [001] interface in zincblende materials $L_{\text{if}} = a/2$, where a is the bulk lattice constant.

Since the interface region is small and the envelope functions are slowly varying, the details of the variations of the $[u_m|V|u_n]_{\mathbf{R}}$ are not of primary importance—it is only the integral of this term over the interface region that determines its role in the envelope Hamiltonian. In the flat interface model, the pseudopotentials are modeled to be equal to those of material A at one side of the interface and moving sharply to those of material B at the other side of an interface. We then obtain:

$$\begin{aligned}\int_{-L_{\text{if}}/2}^{+L_{\text{if}}/2}[u_m|H|u_n]_{z_0}\mathrm{d}z_0 = &\int_{-L_{\text{if}}/2}^{+L_{\text{if}}/2}[u_m|\frac{p^2}{2m_0}+V|u_n]_{z_0}\mathrm{d}z_0\\ &-[u_m|\frac{p^2}{2m_0}+\frac{V_{\text{A}}+V_{\text{B}}}{2}|u_n]L_{\text{if}}+\\ &+[u_m|\frac{p^2}{2m_0}+V_{\text{A}}|u_n]\frac{L_{\text{if}}}{2}+[u_m|\frac{p^2}{2m_0}+V_{\text{B}}|u_n]\frac{L_{\text{if}}}{2}.\end{aligned} \tag{3.8}$$

In Eq. (3.8), the last two terms on the right hand side represent the bulk contribution to the Hamiltonian, while the first two terms are the interface contribution. This implies that for each interface, the envelope function Hamiltonian contains an additional term of the form $\Omega_{mn}\delta(z)$ (assuming the plane of the interface is the $z = 0$ plane), with Ω_{mn} given by the expression:

$$\Omega_{mn} = \int_{-L_{\text{if}}/2}^{+L_{\text{if}}/2}[u_m|\frac{p^2}{2m_0}+V|u_n]_{z_0}\mathrm{d}z_0 - [u_m|\frac{p^2}{2m_0}+\frac{V_{\text{A}}+V_{\text{B}}}{2}|u_n]L_{\text{if}}. \tag{3.9}$$

When one chooses the bulk reference crystal as a virtual crystal being the "average" of crystals A and B, the last expression reduces to

$$\Omega_{mn} = \int_{-L_{\text{if}}/2}^{+L_{\text{if}}/2}[u_m|\frac{p^2}{2m_0}+V|u_n]_{z_0}\mathrm{d}z_0 - E_m\delta_{mn}L_{\text{if}}, \tag{3.10}$$

where E_m is the energy of the band m at the Γ point, and u_m is the corresponding Bloch functions. In the case of square-based pyramid with base width to height ratio $b/h = 2$, the total interface contribution to the Hamiltonian is

$$\begin{aligned} H_{\text{if}} = & \Omega([001])\delta\theta(z) \\ & + \Omega([101])\delta\theta(\mathbf{r}\cdot\mathbf{n}_1 - l) + \Omega([011])\delta\theta(\mathbf{r}\cdot\mathbf{n}_2 - l) \\ & + \Omega([\bar{1}01])\delta\theta(\mathbf{r}\cdot\mathbf{n}_3 - l) + \Omega([0\bar{1}1])\delta\theta(\mathbf{r}\cdot\mathbf{n}_4 - l). \end{aligned} \tag{3.11}$$

In the above equation, $\delta\theta(z)$ function represents the delta function at a given interface, with an additional constraint that the function is nonzero only at the face of the pyramid. The vectors $\mathbf{n}_i$ are the unit vectors perpendicular to the faces of the pyramid and are given as $\mathbf{n}_1 = 1/\sqrt{2}\cdot(1,0,1)$, $\mathbf{n}_2 = 1/\sqrt{2}\cdot(0,1,1)$, $\mathbf{n}_3 = 1/\sqrt{2}\cdot(-1,0,1)$, $\mathbf{n}_4 = 1/\sqrt{2}\cdot(0,-1,1)$ and $l = b/(2\sqrt{2})$. The choice of the coordinate system was made in such a way that the vertices of the pyramid are at the points $(b/2,-b/2,0)$, $(b/2,b/2,0)$, $(-b/2,b/2,0)$, $(-b/2,-b/2,0)$ and $(0,0,h)$.

The explicit form of the matrices Ω can be obtained from density functional theory or empirical pseudopotential calculations. The reader is referred to [83] for a detailed description of the extraction of the matrices Ω from empirical pseudopotentials, while the final results, in the basis $|s_a\rangle, |p_{x,b}\rangle, |p_{y,b}\rangle, |p_{z,b}\rangle$ (see Sect. 3.5 for the meaning of this basis), are given as:

$$\Omega([001]) = \begin{pmatrix} 0 & 0 & 0 & -a \\ & 0 & b & 0 \\ & & 0 & 0 \\ & & & 0 \end{pmatrix}, \tag{3.12}$$

$$\Omega([101]) = \begin{pmatrix} 0 & -c & 0 & -c \\ & 0 & d & 0 \\ & & 0 & d \\ & & & 0 \end{pmatrix}, \tag{3.13}$$

$$\Omega([011]) = \begin{pmatrix} 0 & 0 & -c & -c \\ & 0 & d & d \\ & & 0 & 0 \\ & & & 0 \end{pmatrix}, \tag{3.14}$$

$$\Omega([\bar{1}01]) = \begin{pmatrix} 0 & c & 0 & -c \\ & 0 & d & 0 \\ & & 0 & -d \\ & & & 0 \end{pmatrix}, \tag{3.15}$$

Table 3.1 Relevant material parameters of the interfaces: InAs/GaAs and GaAs/$Al_{0.35}Ga_{0.65}As$

	InAs/GaAs	GaAs/$Al_{0.35}Ga_{0.65}As$
a [eVÅ]	0.61220	0.14899
b [eVÅ]	−0.36633	0.02861
c [eVÅ]	−0.32427	−0.07039
d [eVÅ]	0.02855	0.00008

$$\Omega([0\bar{1}1]) = \begin{pmatrix} 0 & 0 & c & -c \\ & 0 & d & -d \\ & & 0 & 0 \\ & & & 0 \end{pmatrix}. \tag{3.16}$$

The relevant parameters, a, b, c and d, for two representative interfaces InAs/GaAs and GaAs/$Al_{0.35}Ga_{0.65}As$ are given in Table 3.1.

3.4 Symmetry of the Interface Hamiltonian

Proper understanding of the Hamiltonian symmetry group is of great importance for several reasons: (a) symmetry can be used to reduce the computational cost; (b) symmetry induces selection rules for certain physical processes, such as for example light absorption and emission. For this reason, we analyze the influence of the interface Hamiltonians introduced in Sect. 3.3 on the symmetry of the system. The Hamiltonian for the [001] interface in the basis $|s_a\rangle, |p_{x,b}\rangle, |p_{y,b}\rangle, |p_{z,b}\rangle$ reads:

$$H_{[001]} = \begin{pmatrix} 0 & 0 & 0 & -a \\ & 0 & b & 0 \\ & & 0 & 0 \\ & & & 0 \end{pmatrix} \delta\theta(z). \tag{3.17}$$

To represent the actions of the rotation operators on the envelope function spinors, it is more convenient to work in the basis of eigenstates of the z-component of the orbital quasi-angular momentum

$$\{u_1, \ldots, u_4\} = \{|s_a\rangle, \frac{1}{\sqrt{2}}\left(|p_{x,b}\rangle + i\,|p_{y,b}\rangle\right), \frac{1}{\sqrt{2}}\left(|p_{x,b}\rangle - i\,|p_{y,b}\rangle\right), |p_{z,b}\rangle\}. \tag{3.18}$$

In this basis, the same Hamiltonian, $H_{[001]}$, reads

$$H_{[001]} = \begin{pmatrix} 0 & 0 & 0 & -a \\ & 0 & -ib & 0 \\ & & 0 & 0 \\ & & & 0 \end{pmatrix} \delta\theta(z). \tag{3.19}$$

The action of the representation of the rotation R_φ, where $\varphi = n\pi/2$ on the spinors is given as

$$D(R_\varphi)\begin{pmatrix}\psi_1(\mathbf{r})\\ \psi_2(\mathbf{r})\\ \psi_3(\mathbf{r})\\ \psi_4(\mathbf{r})\end{pmatrix} = \begin{pmatrix}\psi_1(R_\varphi\mathbf{r})\\ e^{-i\varphi}\psi_2(R_\varphi\mathbf{r})\\ e^{i\varphi}\psi_3(R_\varphi\mathbf{r})\\ \psi_4(R_\varphi\mathbf{r})\end{pmatrix}. \tag{3.20}$$

To prove that $D(R_\varphi)$ commutes with $H_{[001]}$ it is sufficient to show that operators $H_{[001]}D(R_\varphi)$ and $D(R_\varphi)H_{[001]}$ give the same result when acting on the basis states $(e^{i\mathbf{k}\cdot\mathbf{r}},0,0,0)^\top$, $(0,e^{i\mathbf{k}\cdot\mathbf{r}},0,0)^\top$, $(0,0,e^{i\mathbf{k}\cdot\mathbf{r}},0)^\top$, $(0,0,0,e^{i\mathbf{k}\cdot\mathbf{r}})^\top$ that span the Hilbert space of spinors. By explicitly performing the calculation one obtains:

$$H_{[001]}D(R_\varphi)\begin{pmatrix}0\\ e^{i\mathbf{k}\cdot\mathbf{r}}\\ 0\\ 0\end{pmatrix} = H_{[001]}\begin{pmatrix}0\\ e^{-i\varphi}e^{i(R_\varphi^{-1}\mathbf{k})\cdot\mathbf{r}}\\ 0\\ 0\end{pmatrix} = \begin{pmatrix}0\\ 0\\ ibe^{-i\varphi}\\ 0\end{pmatrix} e^{i(R_\varphi^{-1}\mathbf{k})\cdot\mathbf{r}}\delta\theta(z) \tag{3.21}$$

and on the other hand

$$D(R_\varphi)H_{[001]}\begin{pmatrix}0\\ e^{i\mathbf{k}\cdot\mathbf{r}}\\ 0\\ 0\end{pmatrix} = \begin{pmatrix}0\\ 0\\ ib\\ 0\end{pmatrix} e^{i\mathbf{k}\cdot\mathbf{r}}\delta\theta(z) = \begin{pmatrix}0\\ 0\\ ibe^{i\varphi}\\ 0\end{pmatrix} e^{i(R_\varphi^{-1}\mathbf{k})\cdot\mathbf{r}}\delta\theta(z). \tag{3.22}$$

This implies that $D(R_\varphi)$ and $H_{[001]}$ commute only if $\varphi = n\pi$.

Next, we proceed with the proof that $H_{[001]}$ commutes with the operator $D(\sigma_v)$. For this proof, it is convenient to work in the basis

$$\{u_1,\ldots,u_4\} = \{|s_a\rangle, \frac{1}{\sqrt{2}}\left(|p_{x,b}\rangle + |p_{y,b}\rangle\right), \frac{1}{\sqrt{2}}\left(|p_{x,b}\rangle - |p_{y,b}\rangle\right), |p_{z,b}\rangle\}. \tag{3.23}$$

In this basis $H_{[001]}$ reads

$$H_{[001]} = \begin{pmatrix}0 & 0 & 0 & -a\\ b & 0 & 0 & \\ & -b & 0 & \\ & & 0 & \end{pmatrix}\delta\theta(z), \tag{3.24}$$

while the action of the operator $D(\sigma_v)$ on the spinor is given as

$$D(\sigma_v)\begin{pmatrix}\psi_1(x,y,z)\\ \psi_2(x,y,z)\\ \psi_3(x,y,z)\\ \psi_4(x,y,z)\end{pmatrix} = \begin{pmatrix}\psi_1(y,x,z)\\ \psi_2(y,x,z)\\ -\psi_3(y,x,z)\\ \psi_4(y,x,z)\end{pmatrix}. \tag{3.25}$$

It follows

$$H_{[001]}D(\sigma_v)\begin{pmatrix}0\\0\\e^{i\mathbf{k}\cdot\mathbf{r}}\\0\end{pmatrix} = H_{[001]}\begin{pmatrix}0\\0\\-e^{i(k_xy+k_yx+k_zz)}\\0\end{pmatrix} = \begin{pmatrix}0\\0\\b\\0\end{pmatrix} e^{i(k_xy+k_yx+k_zz)}\delta\theta(z). \tag{3.26}$$

On the other hand

$$D(\sigma_v)H_{[001]}\begin{pmatrix}0\\0\\e^{i\mathbf{k}\cdot\mathbf{r}}\\0\end{pmatrix} = D(\sigma_v)\begin{pmatrix}0\\0\\-b\\0\end{pmatrix}\delta\theta(z)e^{i\mathbf{k}\cdot\mathbf{r}} = \begin{pmatrix}0\\0\\b\\0\end{pmatrix} e^{i(k_xy+k_yx+k_zz)}\delta\theta(z). \tag{3.27}$$

In this way we proved that the symmetry of the interface Hamiltonian, $H_{[001]}$, is C_{2v}. Similarly, it can be shown that the symmetry of $H_{[110]} + H_{[1\bar{1}0]} + H_{[\bar{1}\bar{1}0]} + H_{[\bar{1}10]}$ term is C_{2v} too. Consequently, if the interface effects are included, the symmetry of the model will be reduced from an artificially high C_{4v} to correct C_{2v}.

3.5 The 14-Band k·p Hamiltonian

In the previous section, we have demonstrated that the inclusion of interface effects leads to the correct symmetry of the model. In this section, we will analyze how the inclusion of bands beyond the standard 8 bands affects the symmetry. For this purpose, we will investigate the 14-band Hamiltonian which includes the second conduction band Γ_{5c} (see Fig. 3.1) in addition to the standard 8 bands.

The 14-band **k·p** Hamiltonian in the basis that consists of states that originate from p bonding and antibonding (denoted as p_b and p_a) and s antibonding (denoted as s_a) states of the atoms in the bulk, see Fig. 3.1:

$$\begin{aligned}\{\ &|p_{x,a}\uparrow\rangle, |p_{y,a}\uparrow\rangle, |p_{z,a}\uparrow\rangle, |s_a\uparrow\rangle, |p_{x,b}\uparrow\rangle, |p_{y,b}\uparrow\rangle, |p_{z,b}\uparrow\rangle,\\ &|p_{x,a}\downarrow\rangle, |p_{y,a}\downarrow\rangle, |p_{z,a}\downarrow\rangle, |s_a\downarrow\rangle, |p_{x,b}\downarrow\rangle, |p_{y,b}\downarrow\rangle, |p_{z,b}\downarrow\rangle\},\end{aligned} \tag{3.28}$$

where $\uparrow$ and $\downarrow$ denote spin-up and spin-down states respectively, reads

$$H = \begin{pmatrix} |\uparrow\rangle & |\downarrow\rangle \\ G & 0 \\ 0 & G \end{pmatrix} + \begin{pmatrix} |\uparrow\rangle & |\downarrow\rangle \\ G_{\mathrm{so}} & \Gamma \\ -\Gamma^* & G^*_{\mathrm{so}} \end{pmatrix}, \tag{3.29}$$

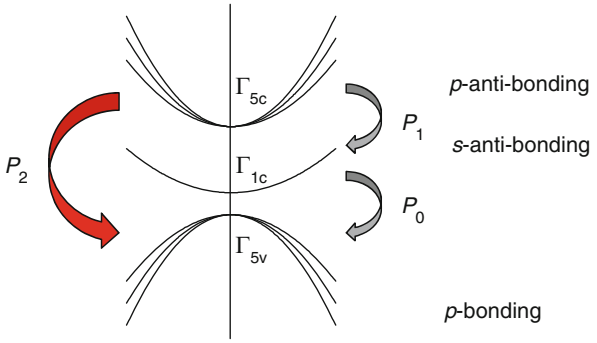

Fig. 3.1 The scheme of the band structure of the material with zincblende crystal structure around the Γ point in the first Brillouin zone, including the coupling elements between the relevant bands in the 14-band **k**·**p** Hamiltonian

where

$$G = \begin{pmatrix} |p_{x,a}\rangle & |p_{y,a}\rangle & |p_{z,a}\rangle & |s_a\rangle & |p_{x,b}\rangle & |p_{y,b}\rangle & |p_{z,b}\rangle \\ E_{p_a} & 0 & 0 & iP_1k_x & 0 & -iP_2k_z & -iP_2k_y \\ & E_{p_a} & 0 & iP_1k_y & -PiP_2k_z & 0 & -iP_2k_x \\ & & E_{p_a} & iP_1k_z & -iP_2k_y & -iP_2k_x & 0 \\ & & & E_{s_a} & iP_0k_x & iP_0k_y & iP_0k_z \\ & & & & E_{p_{x,b}} & W_1 & W_2 \\ & & & & & E_{p_{y,b}} & W_3 \\ & & & & & & E_{p_{z,b}} \end{pmatrix}, \tag{3.30}$$

$$G_{\mathrm{so}} = \begin{pmatrix} |p_{x,a}\rangle & |p_{y,a}\rangle & |p_{z,a}\rangle & |s_a\rangle & |p_{x,b}\rangle & |p_{y,b}\rangle & |p_{z,b}\rangle \\ \frac{2}{3}\Delta_{\mathrm{so}}(p_a) & -\frac{i}{3}\Delta_{\mathrm{so}}(p_a) & 0 & 0 & 0 & \frac{i}{3}\Delta_{\mathrm{cf}} & 0 \\ & \frac{2}{3}\Delta_{\mathrm{so}}(p_a) & 0 & 0 & -\frac{i}{3}\Delta_{\mathrm{cf}} & 0 & 0 \\ & & \frac{2}{3}\Delta_{\mathrm{so}}(p_a) & 0 & 0 & 0 & 0 \\ & & & 0 & 0 & 0 & 0 \\ & & & & -\frac{1}{3}\Delta_{\mathrm{so}}(p_b) & -\frac{i}{3}\Delta_{\mathrm{so}}(p_b) & 0 \\ & & & & & -\frac{1}{3}\Delta_{\mathrm{so}}(p_b) & 0 \\ & & & & & & -\frac{1}{3}\Delta_{\mathrm{so}}(p_b) \end{pmatrix}$$

and

$$\Gamma = \begin{pmatrix} |p_{x,a}\rangle & |p_{y,a}\rangle & |p_{z,a}\rangle & |s_a\rangle & |p_{x,b}\rangle & |p_{y,b}\rangle & |p_{z,b}\rangle \\ 0 & 0 & \frac{1}{3}\Delta_{\mathrm{so}}(p_a) & 0 & 0 & 0 & -\frac{1}{3}\Delta_{\mathrm{cf}} \\ 0 & 0 & -\frac{i}{3}\Delta_{\mathrm{so}}(p_a) & 0 & 0 & 0 & \frac{i}{3}\Delta_{\mathrm{cf}} \\ -\frac{1}{3}\Delta_{\mathrm{so}}(p_a) & \frac{i}{3}\Delta_{\mathrm{so}}(p_a) & 0 & 0 & \frac{1}{3}\Delta_{\mathrm{cf}} & -\frac{i}{3}\Delta_{\mathrm{cf}} & 0 \\ 0 & 0 & 0 & 0 & 0 & 0 & 0 \\ 0 & 0 & -\frac{1}{3}\Delta_{\mathrm{cf}} & 0 & 0 & 0 & \frac{1}{3}\Delta_{\mathrm{so}}(p_b) \\ 0 & 0 & \frac{i}{3}\Delta_{\mathrm{cf}} & 0 & 0 & 0 & -\frac{i}{3}\Delta_{\mathrm{so}}(p_b) \\ \frac{1}{3}\Delta_{\mathrm{cf}} & -\frac{i}{3}\Delta_{\mathrm{cf}} & 0 & 0 & -\frac{1}{3}\Delta_{\mathrm{so}}(p_b) & \frac{i}{3}\Delta_{\mathrm{so}}(p_b) & 0 \end{pmatrix}.$$

The terms in the previous equations are given as:

$$E_{p_a} = E(\Gamma_{5c}), \qquad E_{s_a} = E(\Gamma_{1c}) + \left(\frac{\hbar^2}{2m_0}\right)\gamma_c k^2$$

$$E_{p_{x,b}} = E(\Gamma_{5v}) - (P+Q) - \frac{\sqrt{3}}{2}(R^* + R),$$

$$E_{p_{y,b}} = E(\Gamma_{5v}) - (P+Q) + \frac{\sqrt{3}}{2}(R^* + R)$$

$$E_{p_{z,b}} = E(\Gamma_{5v}) - (P-2Q), \qquad E_{g0} = E(\Gamma_{1c}) - E(\Gamma_{5v}),$$

$$E_{g1} = E(\Gamma_{5c}) - E(\Gamma_{5v})$$

$$W_1 = -i\frac{\sqrt{3}}{2}(R - R^*), \qquad W_2 = -\frac{\sqrt{3}}{2}(S + S^*), \qquad W_3 = -i\frac{\sqrt{3}}{2}(S - S^*)$$

$$P = P_k + P_\epsilon, \qquad Q = Q_k + Q_\epsilon, \qquad R = R_k + R_\epsilon, \qquad S = S_k + S_\epsilon$$

$$P_k = \left(\frac{\hbar^2}{2m_0}\right)\gamma_1(k_x^2 + k_y^2 + k_z^2), \qquad Q_k = \left(\frac{\hbar^2}{2m_0}\right)\gamma_2(k_x^2 + k_y^2 - 2k_z^2)$$

$$R_k = \left(\frac{\hbar^2}{2m_0}\right)\sqrt{3}[\gamma_2(k_x^2 - k_y^2) - 2i\gamma_3 k_x k_y], \quad S_k = \left(\frac{\hbar^2}{2m_0}\right)\sqrt{6}\gamma_3(k_x - ik_y)k_z$$

$$P_\epsilon = -a_v(\epsilon_{xx} + \epsilon_{yy} + \epsilon_{zz}), \qquad Q_\epsilon = -\frac{b_{ax}}{2}(\epsilon_{xx} + \epsilon_{yy} - 2\epsilon_{zz})$$

$$R_\epsilon = -\frac{\sqrt{3}}{2}b_{ax}(\epsilon_{xx} - \epsilon_{yy}) + i\,d_{ax}\epsilon_{xy}, \qquad S_\epsilon = -\frac{d_{ax}}{\sqrt{2}}(\epsilon_{zx} - i\epsilon_{yz})$$

$$E_{P0} = 2m_0 P_0^2/\hbar^2, \qquad E_{P1} = 2m_0 P_1^2/\hbar^2, \qquad E_{P2} = 2m_0 P_2^2/\hbar^2$$

$$\begin{aligned}\gamma_c =& \frac{1}{m^*} - \frac{E_{P0}}{3}\left[\frac{2}{E_{g0}} + \frac{1}{E_{g0} + \Delta_{\rm so}(p_b)}\right] \\ &+ \frac{E_{P1}}{3}\left[\frac{1}{E_{g1} - E_{g0}} + \frac{2}{E_{g1} - E_{g0} + \Delta_{\rm so}(p_a)}\right],\end{aligned}$$

$$\gamma_1 = \gamma_1^L - \frac{1}{3}\frac{E_{P0}}{E_{g0} + \Delta_{\rm so}(p_b)/3} - \frac{2}{3}\frac{E_{P2}}{E_{g1} + \Delta_{\rm so}(p_b)/3 + 2\Delta_{\rm so}(p_a)/3},$$

$$\gamma_2 = \gamma_2^L - \frac{1}{6}\frac{E_{P0}E_{g0} + \Delta_{\rm so}(p_b)/3}{+}\frac{1}{6}\frac{E_{P2}}{E_{g1} + \Delta_{\rm so}(p_b)/3 + 2\Delta_{\rm so}(p_a)/3},$$

$$\gamma_3 = \gamma_3^L - \frac{1}{6}\frac{E_{P0}E_{g0} + \Delta_{\rm so}(p_b)/3}{-}\frac{1}{6}\frac{E_{P2}}{E_{g1} + \Delta_{\rm so}(p_b)/3 + 2\Delta_{\rm so}(p_a)/3}.$$

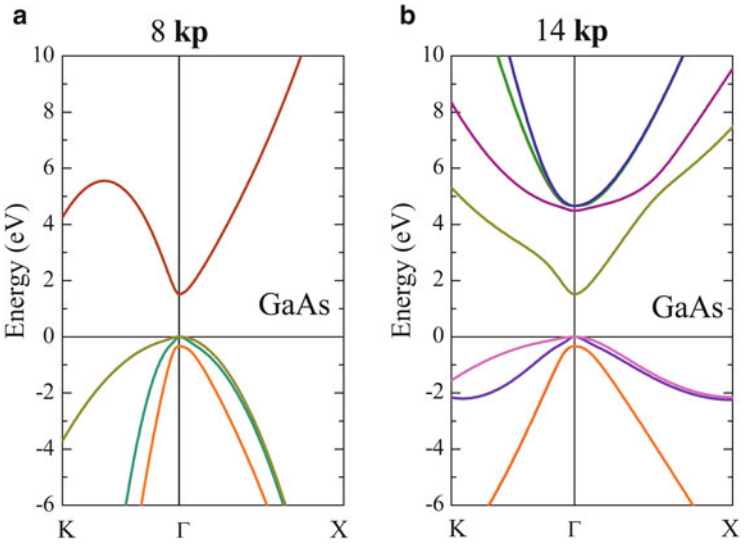

Fig. 3.2 Electronic structure of unstrained GaAs bulk material calculated using the 8-band **k·p** (**a**) and 14-band **k·p** (**b**) Hamiltonian along K–Γ–X path in the first Brillouin zone

$E(\Gamma_{5c})$, $E(\Gamma_{1c})$, $E(\Gamma_{5v})$ are the bulk band energies at the Γ point, m_0 the electron mass, $\hbar$ the reduced Planck's constant, k_x, k_y, k_z denote the components of the wave vector along the crystallographic directions [100], [010], and [001] in the vicinity of the Γ point, P_0, P_1, P_2 are the momentum matrix elements between Γ_{1c} and Γ_{5v}, Γ_{5c} and Γ_{1c}, and Γ_{5c} and Γ_{5v} states respectively, E_{P0}, E_{P1}, E_{P2} are the Kane energies related to P_0, P_1 and P_2 respectively, $\gamma_1^L, \gamma_2^L, \gamma_3^L$ are the Luttinger parameters, m^* is the effective mass in the conduction band, $\Delta_{\mathrm{SO}}(p_b)$ is the spin-orbit splitting between p-bonding states in the valence band, $\Delta_{\mathrm{SO}}(p_a)$ is the spin-orbit splitting between p-antibonding states in the conduction band, Δ_{cf} is the crystal field splitting, ϵ_{ij} are the strain tensor components, a_c and a_v are the conduction band and valence band hydrostatic deformation potentials respectively, b_{ax} and d_{ax} are the shear deformation potentials along the [001] and [111] direction respectively. The values of relevant material parameters are given in the Appendix.

In Fig. 3.2 we plot the electronic structure of unstrained GaAs calculated using the 8-band **k·p** (a) and 14-band **k·p** (b) Hamiltonian along the K–Γ–X path in the first Brillouin zone. It is visible that additional band couplings in the 14-band **k·p** Hamiltonian prevent dangerous appearance of spurious solutions that might exist in the 8-band **k·p** Hamiltonian. These spurious solutions in the 8-band **k·p** Hamiltonian are related to appearance of the artificial folding points in the lowest conduction band due to small basis size of such a Hamiltonian.

3.6 Symmetry of the 14-Band k·p Hamiltonian

3.6.1 *Symmetry of the 8-Band* k·p *Hamiltonian*

To establish the symmetry of the kinetic part of the 14-band **k·p** Hamiltonian we start with the analysis of the 8-band **k·p** Hamiltonian, which is a constituent part of the 14-band Hamiltonian. The kinetic part of the 8-band **k·p** Hamiltonian consists of two identical uncoupled 4×4 blocks. In the basis

$$\{u_1, \ldots, u_4\} = \{|s_a\rangle, |p_{x,b}\rangle, |p_{y,b}\rangle, |p_{z,b}\rangle\} \tag{3.31}$$

these blocks read:

$$H_4 = \begin{pmatrix} E_c(\mathbf{r}) & ik_x P_0 & ik_y P_0 & ik_z P_0 \\ & E_v(\mathbf{r}) & 0 & 0 \\ & & E_v(\mathbf{r}) & 0 \\ & & & E_v(\mathbf{r}) \end{pmatrix}, \tag{3.32}$$

where $E_c(\mathbf{r}) = E_{s_a}(\mathbf{r})$ and $E_v(\mathbf{r}) = E_{p_b}(\mathbf{r})$. In (3.32), the effect of remote bands was not included as its inclusion does not affect the symmetry considerations. We will show that this Hamiltonian applied to square-based pyramidal quantum dots has C_{4v} symmetry. To do this, it is sufficient to show that the blocks H_4 commute with the generators of the group—the rotation $R_{\pi/2}$ and the reflection σ_v.

To represent the actions of the rotation operators on the envelope function spinors, it is more convenient to work in the basis of eigenstates of the z-component of the orbital quasi-angular momentum (3.18) where the block H_4 reads

$$H_4 = \begin{pmatrix} E_c(\mathbf{r}) & ik_+ P_0 & ik_- P_0 & ik_z P_0 \\ & E_v(\mathbf{r}) & 0 & 0 \\ & & E_v(\mathbf{r}) & 0 \\ & & & E_v(\mathbf{r}) \end{pmatrix}, \tag{3.33}$$

where $k_\pm = \frac{1}{\sqrt{2}}\left(k_x \pm ik_y\right)$. The action of the representation of the rotation R_φ, where $\varphi = n\pi/2$ on the spinors is given by (3.20).

To prove that $D(R_\varphi)$ commutes with H_4 it is sufficient to show that operators $H_4 D(R_\varphi)$ and $D(R_\varphi) H_4$ give the same result when acting on the basis states $(e^{i\mathbf{k}\cdot\mathbf{r}}, 0, 0, 0)^\top$, $(0, e^{i\mathbf{k}\cdot\mathbf{r}}, 0, 0)^\top$, $(0, 0, e^{i\mathbf{k}\cdot\mathbf{r}}, 0)^\top$, $(0, 0, 0, e^{i\mathbf{k}\cdot\mathbf{r}})^\top$ that span the Hilbert space of spinors. By explicitly performing the calculation one gets on the one hand

$$H_4 D(R_\varphi) \begin{pmatrix} e^{i\mathbf{k}\cdot\mathbf{r}} \\ 0 \\ 0 \\ 0 \end{pmatrix} = H_4 \begin{pmatrix} e^{i(R_\varphi^{-1}\mathbf{k})\cdot\mathbf{r}} \\ 0 \\ 0 \\ 0 \end{pmatrix} = \begin{pmatrix} E_c(\mathbf{r}) \\ -iP_0(R_\varphi^{-1}\mathbf{k})_- \\ -iP_0(R_\varphi^{-1}\mathbf{k})_+ \\ -iP_0(R_\varphi^{-1}\mathbf{k})_z \end{pmatrix} e^{i(R_\varphi^{-1}\mathbf{k})\cdot\mathbf{r}} \tag{3.34}$$

and on the other hand

$$D(R_\varphi)H_4\begin{pmatrix} e^{i\mathbf{k}\cdot\mathbf{r}} \\ 0 \\ 0 \\ 0 \end{pmatrix} = D(R_\varphi)\begin{pmatrix} E_c(\mathbf{r}) \\ -iP_0k_- \\ -iP_0k_+ \\ -iP_0k_z \end{pmatrix} e^{i\mathbf{k}\cdot\mathbf{r}} = \begin{pmatrix} E_c(R_\varphi\mathbf{r}) \\ e^{-i\varphi}(-i)P_0k_- \\ e^{i\varphi}(-i)P_0k_+ \\ -iP_0k_z \end{pmatrix} e^{i(R_\varphi^{-1}\mathbf{k})\cdot\mathbf{r}}. \tag{3.35}$$

Due to the symmetry of the dot shape it follows that $E_c(\mathbf{r}) = E_c(R_\varphi\mathbf{r})$. Furthermore, one can straightforwardly show that $(R_\varphi^{-1}\mathbf{k})_- = e^{-i\varphi}k_-$ and $(R_\varphi^{-1}\mathbf{k})_+ = e^{i\varphi}k_+$. From these identities, it follows that

$$\left[D(R_\varphi)H_4 - H_4D(R_\varphi)\right]\begin{pmatrix} e^{i\mathbf{k}\cdot\mathbf{r}} \\ 0 \\ 0 \\ 0 \end{pmatrix} = 0. \tag{3.36}$$

Using the same procedure, one can also show that $D(R_\varphi)H_4$ and $H_4D(R_\varphi)$ give the same result when acting on the other basis vectors $(0, e^{i\mathbf{k}\cdot\mathbf{r}}, 0, 0)^\top$, $(0, 0, e^{i\mathbf{k}\cdot\mathbf{r}}, 0)^\top$, $(0, 0, 0, e^{i\mathbf{k}\cdot\mathbf{r}})^\top$, which completes the proof that $D(R_\varphi)H_4$ and $H_4D(R_\varphi)$ commute.

Next, we proceed with the proof that H_4 commutes with the operator $D(\sigma_v)$. For this proof, it is convenient to work in the basis (3.23). The Hamiltonian in this basis reads

$$H_4 = \begin{pmatrix} E_c(\mathbf{r}) & i\frac{1}{\sqrt{2}}(k_x + k_y)P_0 & i\frac{1}{\sqrt{2}}(k_x - k_y)P_0 & ik_zP_0 \\ & E_v(\mathbf{r}) & 0 & 0 \\ & & E_v(\mathbf{r}) & 0 \\ & & & E_v(\mathbf{r}) \end{pmatrix}. \tag{3.37}$$

In this basis, the action of the operator $D(\sigma_v)$ on the spinor is given by (3.25). It follows

$$H_4D(\sigma_v)\begin{pmatrix} e^{i\mathbf{k}\cdot\mathbf{r}} \\ 0 \\ 0 \\ 0 \end{pmatrix} = H_4\begin{pmatrix} e^{i(k_xy+k_yx+k_zz)} \\ 0 \\ 0 \\ 0 \end{pmatrix} = \begin{pmatrix} E_c(\mathbf{r}) \\ -iP_0\frac{1}{\sqrt{2}}(k_x+k_y) \\ -iP_0\frac{1}{\sqrt{2}}(k_y-k_x) \\ -iP_0k_z \end{pmatrix} e^{i(k_xy+k_yx+k_zz)}. \tag{3.38}$$

On the other hand

$$
\begin{aligned}
D(\sigma_v)H_4\begin{pmatrix} e^{i\mathbf{k}\cdot\mathbf{r}} \\ 0 \\ 0 \\ 0 \end{pmatrix} &= D(\sigma_v)\begin{pmatrix} E_c(\mathbf{r}) \\ -iP_0\frac{1}{\sqrt{2}}(k_x+k_y) \\ -iP_0\frac{1}{\sqrt{2}}(k_x-k_y) \\ -iP_0k_z \end{pmatrix} e^{i\mathbf{k}\cdot\mathbf{r}} \\
&= \begin{pmatrix} E_c(y,x,z) \\ -iP_0\frac{1}{\sqrt{2}}(k_x+k_y) \\ -iP_0\frac{1}{\sqrt{2}}(k_x-k_y)\cdot(-1) \\ -iP_0k_z \end{pmatrix} e^{i(k_xy+k_yx+k_zz)}
\end{aligned}
\tag{3.39}
$$

and consequently

$$
[D(\sigma_v)H_4 - H_4D(\sigma_v)]\begin{pmatrix} e^{i\mathbf{k}\cdot\mathbf{r}} \\ 0 \\ 0 \\ 0 \end{pmatrix} = 0. \tag{3.40}
$$

One can straightforwardly check this equality for other basis vectors $(0, e^{i\mathbf{k}\cdot\mathbf{r}}, 0, 0)^\top$, $(0, 0, e^{i\mathbf{k}\cdot\mathbf{r}}, 0)^\top$, $(0, 0, 0, e^{i\mathbf{k}\cdot\mathbf{r}})^\top$. That completes the proof that the kinetic part of the 8-band $\mathbf{k}\cdot\mathbf{p}$ Hamiltonian is of C_{4v} symmetry.

3.6.2 Symmetry of the Whole 14-Band Hamiltonian

We proceed with the analysis of the kinetic part of the 14-band $\mathbf{k}\cdot\mathbf{p}$ Hamiltonian. This Hamiltonian consists of two uncoupled 7×7 blocks that read (excluding the remote band effects that do not affect the symmetry considerations):

$$
H_7 = \begin{pmatrix}
|p_{x,a}\rangle & |p_{y,a}\rangle & |p_{z,a}\rangle & |s_a\rangle & |p_{x,b}\rangle & |p_{y,b}\rangle & |p_{z,b}\rangle \\
E_{c2}(\mathbf{r}) & 0 & 0 & iP_1k_x & 0 & -iP_2k_z & -iP_2k_y \\
 & E_{c2}(\mathbf{r}) & 0 & iP_1k_y & -iP_2k_z & 0 & -iP_2k_x \\
 & & E_{c2}(\mathbf{r}) & iP_1k_z & -iP_2k_y & -iP_2k_x & 0 \\
 & & & E_c(\mathbf{r}) & iP_0k_x & iP_0k_y & iP_0k_z \\
 & & & & E_v(\mathbf{r}) & 0 & 0 \\
 & & & & & E_v(\mathbf{r}) & 0 \\
 & & & & & & E_v(\mathbf{r})
\end{pmatrix}. \tag{3.41}
$$

where $E_{c2}(\mathbf{r}) = E_{p_a}(\mathbf{r})$. The 4×4 block that contains the elements P_1 is of the same form as H_4 and therefore commutes with the operators that represent the elements of the C_{4v} group. One needs therefore to understand the symmetry properties of the block that contains the P_2 elements only. This block reads:

$$H_7 = \begin{pmatrix} |p_{x,a}\rangle & |p_{y,a}\rangle & |p_{z,a}\rangle & |s_a\rangle & |p_{x,b}\rangle & |p_{y,b}\rangle & |p_{z,b}\rangle \\ 0 & 0 & 0 & 0 & 0 & -iP_2k_z & -iP_2k_y \\ & 0 & 0 & 0 & -iP_2k_z & 0 & -iP_2k_x \\ & & 0 & 0 & -iP_2k_y & -iP_2k_x & 0 \\ & & & 0 & 0 & 0 & 0 \\ & & & & 0 & 0 & 0 \\ & & & & & 0 & 0 \\ & & & & & & 0 \end{pmatrix}. \tag{3.42}$$

The most convenient basis to represent the action of the rotation operators is the basis

$$\begin{aligned} \{u_1, \ldots, u_7\} = \{ & \tfrac{1}{\sqrt{2}} \left(|p_{x,a}\rangle + i\,|p_{y,a}\rangle \right), \tfrac{1}{\sqrt{2}} \left(|p_{x,a}\rangle - i\,|p_{y,a}\rangle \right), |p_{z,a}\rangle, |s_a\rangle, \\ & \tfrac{1}{\sqrt{2}} \left(|p_{x,b}\rangle + i\,|p_{y,b}\rangle \right), \tfrac{1}{\sqrt{2}} \left(|p_{x,b}\rangle - i\,|p_{y,b}\rangle \right), |p_{z,b}\rangle \}. \end{aligned} \tag{3.43}$$

In this basis, the H_7 block reads

$$H_7 = \begin{pmatrix} 0 & 0 & 0 & 0 & 0 & -P_2k_z & -P_2k_+ \\ & 0 & 0 & 0 & P_2k_z & 0 & P_2k_- \\ & & 0 & 0 & P_2k_- & -P_2k_+ & 0 \\ & & & 0 & 0 & 0 & 0 \\ & & & & 0 & 0 & 0 \\ & & & & & 0 & 0 \\ & & & & & & 0 \end{pmatrix}. \tag{3.44}$$

The action of the rotation operator on the spinor is given as

$$D(R_\varphi) \begin{pmatrix} \psi_1(\mathbf{r}) \\ \psi_2(\mathbf{r}) \\ \psi_3(\mathbf{r}) \\ \psi_4(\mathbf{r}) \\ \psi_5(\mathbf{r}) \\ \psi_6(\mathbf{r}) \\ \psi_7(\mathbf{r}) \end{pmatrix} = \begin{pmatrix} e^{-i\varphi}\psi_1(R_\varphi\mathbf{r}) \\ e^{i\varphi}\psi_2(R_\varphi\mathbf{r}) \\ \psi_3(R_\varphi\mathbf{r}) \\ \psi_4(R_\varphi\mathbf{r}) \\ e^{-i\varphi}\psi_5(R_\varphi\mathbf{r}) \\ e^{i\varphi}\psi_6(R_\varphi\mathbf{r}) \\ \psi_7(R_\varphi\mathbf{r}) \end{pmatrix}. \tag{3.45}$$

One then gets on the one hand

$$H_7 D(R_\varphi)\begin{pmatrix} e^{i\mathbf{k}\cdot\mathbf{r}} \\ 0 \\ 0 \\ 0 \\ 0 \\ 0 \\ 0 \end{pmatrix} = H_7 \begin{pmatrix} e^{-i\varphi} e^{i(R_\varphi^{-1}\mathbf{k})\cdot\mathbf{r}} \\ 0 \\ 0 \\ 0 \\ 0 \\ 0 \\ 0 \end{pmatrix} = \begin{pmatrix} 0 \\ 0 \\ 0 \\ 0 \\ 0 \\ -e^{-i\varphi} P_2 (R_\varphi^{-1}\mathbf{k})_z \\ e^{-i\varphi}(-P_2)(R_\varphi^{-1}\mathbf{k})_- \end{pmatrix} e^{i(R_\varphi^{-1}\mathbf{k})\cdot\mathbf{r}} \tag{3.46}$$

and on the other hand

$$D(R_\varphi) H_7 \begin{pmatrix} e^{i\mathbf{k}\cdot\mathbf{r}} \\ 0 \\ 0 \\ 0 \\ 0 \\ 0 \\ 0 \end{pmatrix} = D(R_\varphi) \begin{pmatrix} 0 \\ 0 \\ 0 \\ 0 \\ 0 \\ -P_2 k_z \\ -P_2 k_- \end{pmatrix} e^{i\mathbf{k}\cdot\mathbf{r}} = \begin{pmatrix} 0 \\ 0 \\ 0 \\ 0 \\ 0 \\ -e^{i\varphi} P_2 k_z \\ -P_2 k_- \end{pmatrix} e^{i(R_\varphi^{-1}\mathbf{k})\cdot\mathbf{r}}. \tag{3.47}$$

It then follows that

$$\left[D(R_\varphi) H_7 - H_7 D(R_\varphi)\right] \begin{pmatrix} e^{i\mathbf{k}\cdot\mathbf{r}} \\ 0 \\ 0 \\ 0 \\ 0 \\ 0 \\ 0 \end{pmatrix} = 0 \tag{3.48}$$

only if $e^{i\varphi} = e^{-i\varphi}$, which implies $\varphi = n\pi$. One can further straightforwardly extend this result to other basis vectors.

The most convenient basis to represent the action of the $D(\sigma_v)$ operator is the basis

$$\begin{aligned} \{u_1, \ldots, u_7\} = \{ & \tfrac{1}{\sqrt{2}} \left(|p_{x,a}\rangle + |p_{y,a}\rangle\right), \tfrac{1}{\sqrt{2}} \left(|p_{x,a}\rangle - |p_{y,a}\rangle\right), |p_{z,a}\rangle, |s_a\rangle, \\ & \tfrac{1}{\sqrt{2}} \left(|p_{x,b}\rangle + |p_{y,b}\rangle\right), \tfrac{1}{\sqrt{2}} \left(|p_{x,b}\rangle - |p_{y,b}\rangle\right), |p_{z,b}\rangle\}. \end{aligned} \tag{3.49}$$

In this basis, the H_7 block reads

$$H_7 = \begin{pmatrix} 0 & 0 & 0 & 0 & -iP_2k_z & 0 & \frac{-i}{\sqrt{2}}P_2(k_x+k_y) \\ & 0 & 0 & 0 & 0 & iP_2k_z & \frac{1}{\sqrt{2}}(-i)P_2(k_y-k_x) \\ & & 0 & 0 & \frac{-i}{\sqrt{2}}P_2(k_x+k_y) & \frac{-i}{\sqrt{2}}P_2(k_y-k_x) & 0 \\ & & & 0 & 0 & 0 & 0 \\ & & & & 0 & 0 & 0 \\ & & & & & 0 & 0 \\ & & & & & & 0 \end{pmatrix}. \quad (3.50)$$

In the basis (3.49), the action of the operator $D(\sigma_v)$ on the spinor is given as

$$D(\sigma_v)\begin{pmatrix} \psi_1(x,y,z) \\ \psi_2(x,y,z) \\ \psi_3(x,y,z) \\ \psi_4(x,y,z) \\ \psi_5(x,y,z) \\ \psi_6(x,y,z) \\ \psi_7(x,y,z) \end{pmatrix} = \begin{pmatrix} \psi_1(y,x,z) \\ -\psi_2(y,x,z) \\ \psi_3(y,x,z) \\ \psi_4(y,x,z) \\ \psi_5(y,x,z) \\ -\psi_6(y,x,z) \\ \psi_7(y,x,z) \end{pmatrix}. \quad (3.51)$$

It follows

$$H_7 D(\sigma_v)\begin{pmatrix} e^{i\mathbf{k}\cdot\mathbf{r}} \\ 0 \\ 0 \\ 0 \\ 0 \\ 0 \\ 0 \end{pmatrix} = H_7 \begin{pmatrix} e^{i(k_x y+k_y x+k_z z)} \\ 0 \\ 0 \\ 0 \\ 0 \\ 0 \\ 0 \end{pmatrix}$$

$$= \begin{pmatrix} 0 \\ 0 \\ 0 \\ 0 \\ iP_2k_z \\ 0 \\ \frac{1}{\sqrt{2}}iP_2(k_x+k_y) \end{pmatrix} e^{i(k_x y+k_y x+k_z z)}. \quad (3.52)$$

On the other hand

$$D(\sigma_v)H_7\begin{pmatrix} e^{i\mathbf{k}\cdot\mathbf{r}} \\ 0 \\ 0 \\ 0 \\ 0 \\ 0 \\ 0 \end{pmatrix} = D(\sigma_v)\begin{pmatrix} 0 \\ 0 \\ 0 \\ 0 \\ iP_2k_z \\ 0 \\ \frac{1}{\sqrt{2}}iP_2(k_x+k_y) \end{pmatrix} e^{i\mathbf{k}\cdot\mathbf{r}}$$

$$= \begin{pmatrix} 0 \\ 0 \\ 0 \\ 0 \\ iP_2k_z \\ 0 \\ \frac{1}{\sqrt{2}}iP_2(k_x+k_y) \end{pmatrix} e^{i(k_xy+k_yx+k_zz)} \tag{3.53}$$

and consequently

$$[D(\sigma_v)H_7 - H_7D(\sigma_v)]\begin{pmatrix} e^{i\mathbf{k}\cdot\mathbf{r}} \\ 0 \\ 0 \\ 0 \\ 0 \\ 0 \\ 0 \end{pmatrix} = 0. \tag{3.54}$$

One can further show that this result is valid also for other basis vectors. This completes the proof that the symmetry of the kinetic part of the 14-band $\mathbf{k}\cdot\mathbf{p}$ Hamiltonian is C_{2v}.

3.7 Plane Wave Representation

Within the plane wave method [5, 7, 16, 26, 39, 79, 81], the envelope functions are expanded as a linear combination of plane waves $a_{\boldsymbol{k}}(\boldsymbol{r}) = e^{i\boldsymbol{k}\cdot\boldsymbol{r}}$

$$\psi_b(\boldsymbol{r}) = \sum_{\boldsymbol{k}} A_{b\boldsymbol{k}}a_{\boldsymbol{k}}(\boldsymbol{r}), \tag{3.55}$$

with the goal of finding the coefficients $A_{b\boldsymbol{k}}$ in the expansion. The index b takes the integer values $b \in \{1, \ldots, N_b\}$, where N_b is the number of bands in the multiband Hamiltonian. The $\boldsymbol{k}$-space is discretized by embedding the dot in a rectangular box

of dimensions $L_x^{(e)}$, $L_y^{(e)}$, and $L_z^{(e)}$ (and volume $\Omega^{(e)} = L_x^{(e)} L_y^{(e)} L_z^{(e)}$) and choosing the $\boldsymbol{k}$-vectors in the form $\boldsymbol{k} = 2\pi(n_x/L_x^{(e)}, n_y/L_y^{(e)}, n_z/L_z^{(e)})$, where n_x, n_y and n_z are integers. A wave vector cutoff is typically made by imposing the conditions $|n_x| \leq m_x^{(e)}$, $|n_y| \leq m_y^{(e)}$, and $|n_z| \leq m_z^{(e)}$ for all bands.

After making the substitution of (3.55) into the Hamiltonian eigenvalue problem one gets

$$\sum_{b\boldsymbol{k}} \mathscr{H}_{ib}(\boldsymbol{q}, \boldsymbol{k}) A_{b\boldsymbol{k}} = E A_{i\boldsymbol{q}}, \tag{3.56}$$

where

$$\mathscr{H}_{ib}(\boldsymbol{q}, \boldsymbol{k}) = \frac{1}{\Omega^{(e)}} \int_{\Omega^{(e)}} \mathrm{d}^3 \boldsymbol{r}\, a_{\boldsymbol{q}}(\boldsymbol{r})^* h_{ib} a_{\boldsymbol{k}}(\boldsymbol{r}). \tag{3.57}$$

Several characteristics have contributed to the popularity of the plane wave method: plane-wave representation of all operators in the envelope Hamiltonian is analytical, strain distribution can be calculated analytically in Fourier space [4], and a relatively small number of plane waves is sufficient for good accuracy.

The reader interested in other numerical methods for solving the eigenvalue problem of multiband Hamiltonian, such as the finite difference method [29, 47, 56, 76] and other wave function expansion methods (where the eigenfunctions of the particle in a cylinder with infinite walls [46, 77] or eigenfunctions of a harmonic oscillator [66] are used as basis set) is referred to relevant literature.

However, there is one serious shortcoming of the plane wave method when its application to single quantum dot structures is concerned: it inherently assumes periodic boundary conditions. In such a way, it artificially introduces translational symmetry of the system. This leads to artificial physical interaction of a quantum dot with its periodically replicated images through: (a) electronic coupling between states of neighboring dots; (b) propagation of strain field of neighboring dots; (c) Coulomb interaction between carrier in the dot with carriers in its artificial images.

Let the length scales where electronic coupling, strain field and Coulomb interactions become negligible respectively be $L^{(e)}$, $L^{(s)}$ and $L^{(c)}$, see Fig. 3.3 for notation. The wave function decays exponentially away from the dot, the strain field has a slower polynomial decay, while the long range Coulomb interaction has the slowest decay. Therefore, the inequality $L^{(e)} < L^{(s)} < L^{(c)}$ holds. In order to eliminate the effects of the interaction with images one would have to choose the embedding box of dimensions $L^{(c)}$ which can be quite large. This leads to the necessity of using a larger number of plane waves to accurately represent the wave function in the quantum dot region, which is undesirable since a large matrix needs to be diagonalized then.

We will show in the next section that the embedding box of the dimensions $L^{(e)}$ can still be used provided that a proper modification in the calculation procedure is performed.

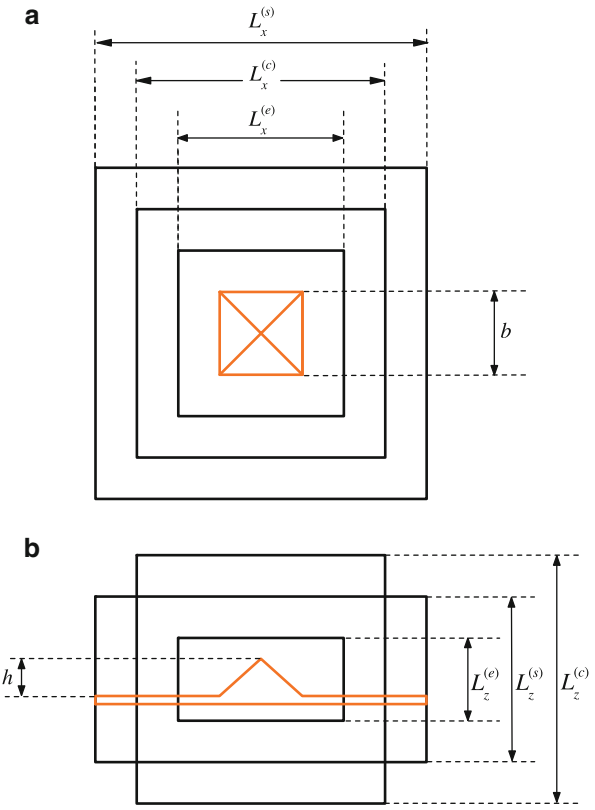

Fig. 3.3 Top view (**a**) and side view (**b**), schematic diagram of an InAs/GaAs quantum dot in the shape of a pyramid, embedded in three "Russian doll" type nested embedding boxes that are used for electronic structure [superscript (e)], strain [superscript (s)] and Coulomb integral calculations [superscript (c)], as described in the main text

3.8 Removal of Artificial Translational Symmetry Effects in Plane Wave Calculations

The essential quantities needed for the description of few particle states (such as excitons and multiexcitons) in quantum dots are the Coulomb integrals. The Coulomb integral among the states i, j, k and l is defined as

$$V_{ijkl} = \sum_{b=1}^{N_b} \sum_{b'=1}^{N_b} \int_{\Omega}^{(\mathrm{e})} \mathrm{d}^3\boldsymbol{r} \int_{\Omega}^{(\mathrm{e})} \mathrm{d}^3\boldsymbol{r}' \psi_b^{(i)}(\boldsymbol{r})^* \psi_b^{(j)}(\boldsymbol{r}) V(|\boldsymbol{r}-\boldsymbol{r}'|) \psi_{b'}^{(k)}(\boldsymbol{r}')^* \psi_{b'}^{(l)}(\boldsymbol{r}') \tag{3.58}$$

where

$$V(u) = \frac{e^2}{4\pi\varepsilon u},$$

with ε being the static dielectric constant. The integral in Eq. (3.58) can be rewritten as

$$V_{ijkl} = \int_{\Omega}^{(e)} \mathrm{d}^3\boldsymbol{r} \int_{\Omega}^{(e)} \mathrm{d}^3\boldsymbol{r}' B_{ij}(\boldsymbol{r}) V(|\boldsymbol{r} - \boldsymbol{r}'|) B_{kl}(\boldsymbol{r}'), \tag{3.59}$$

where

$$B_{ij}(\boldsymbol{r}) = \sum_{b=1}^{N_b} \psi_b^{(i)}(\boldsymbol{r})^* \psi_b^{(j)}(\boldsymbol{r}). \tag{3.60}$$

Next, we define the plane wave expansion of $B_{ij}(\boldsymbol{r})$ as

$$B_{ij}(\boldsymbol{r}) = \sum_{\boldsymbol{q} \in \mathrm{inv}\Omega^{(e)}} B_{ij}(\boldsymbol{q}) e^{i\boldsymbol{q}\cdot\boldsymbol{r}}. \tag{3.61}$$

Replacing the last expression into Eq. (3.59) one obtains

$$V_{ijkl} = \sum_{\boldsymbol{q} \in \mathrm{inv}\Omega^{(e)}} B_{ij}(\boldsymbol{q}) \sum_{\boldsymbol{q}' \in \mathrm{inv}\Omega^{(e)}} B_{kl}(\boldsymbol{q}') \int_{\Omega}^{(e)} \mathrm{d}^3\boldsymbol{r} \int_{\Omega}^{(e)} \mathrm{d}^3\boldsymbol{r}' e^{i\boldsymbol{q}\cdot\boldsymbol{r}} V(|\boldsymbol{r} - \boldsymbol{r}'|) e^{i\boldsymbol{q}'\cdot\boldsymbol{r}'}. \tag{3.62}$$

The $B_{ij}(\boldsymbol{q})$ term can be expressed in terms of the coefficients in the envelope function plane wave expansion as

$$B_{ij}(\boldsymbol{q}) = \sum_{b=1}^{N_b} \sum_{\boldsymbol{q}_1 \in \mathrm{inv}\Omega^{(e)}} A^{(i)*}_{\boldsymbol{q}_1,b} A^{(j)}_{\boldsymbol{q}_1+\boldsymbol{q},b}. \tag{3.63}$$

Next, we introduce an approximation that changes the domain of integration in one of the integrals in Eq. (3.62) from $\Omega^{(e)}$ to the whole space (which is valid when $\Omega^{(e)}$ is large enough) and make the replacement of variables from $\boldsymbol{r}$ and $\boldsymbol{r}'$, to $\boldsymbol{r}$ and $\boldsymbol{u} = \boldsymbol{r} - \boldsymbol{r}'$

$$V^{(\mathrm{a0})}_{ijkl} = \sum_{\boldsymbol{q} \in \mathrm{inv}\Omega^{(e)}} B_{ij}(\boldsymbol{q}) \sum_{\boldsymbol{q}' \in \mathrm{inv}\Omega^{(e)}} B_{kl}(\boldsymbol{q}') \left[\int_{\Omega}^{(e)} \mathrm{d}^3\boldsymbol{r} e^{i\boldsymbol{q}\cdot\boldsymbol{r}} e^{i\boldsymbol{q}'\cdot\boldsymbol{r}} \right] \left[\int \mathrm{d}^3\boldsymbol{u} V(|u|) e^{-i\boldsymbol{q}'\cdot\boldsymbol{u}} \right]. \tag{3.64}$$

Exploiting the relations

$$\int \mathrm{d}^3\boldsymbol{u} e^{-i\boldsymbol{q}'\boldsymbol{u}} V(|u|) = \frac{e^2}{\varepsilon q'^2}$$

and

$$\frac{1}{\Omega^{(e)}}\int_{\Omega}^{(e)} \mathrm{d}^3\boldsymbol{r}\, e^{i(\boldsymbol{q}+\boldsymbol{q}')\boldsymbol{r}} = \delta_{\boldsymbol{q}+\boldsymbol{q}',0}$$

one gets

$$V_{ijkl}^{(\mathrm{a0})} = \Omega^{(e)} \sum_{\substack{\boldsymbol{q}\in \mathrm{inv}\Omega^{(e)} \\ \boldsymbol{q}\neq 0}} B_{ij}(\boldsymbol{q}) B_{kl}(-\boldsymbol{q}) \frac{e^2}{\varepsilon q^2}. \tag{3.65}$$

As already pointed out, $V_{ijkl}^{(\mathrm{a0})}$ is only an approximation to V_{ijkl}. It is therefore very important to understand the nature of error introduced by using Eq. (3.65). One can interpret the initial expression given by Eq. (3.58) as the energy of the electrostatic interaction between the complex charges $B_{ij}(\boldsymbol{r})$ and $B_{kl}(\boldsymbol{r})$, both being located in volume $\Omega^{(e)}$. On the other hand, the expression given by Eq. (3.64) is the energy of the electrostatic interaction between $B_{ij}(\boldsymbol{r})$ located in volume $\Omega^{(e)}$ and $B_{kl}(\boldsymbol{r})$, located in the whole space with periodicity of the box $\Omega^{(e)}$. As a consequence, the error that is introduced by calculating V_{ijkl} using Eq. (3.65) stems from the interactions among the charge $B_{ij}(\boldsymbol{r})$ of a single quantum dot and periodically replicated charges $B_{kl}(\boldsymbol{r})$ of neighboring periodically replicated array of dots.

Now that we understand the nature of error in Eq. (3.65), we can develop a way to systematically correct it. We define the functions $B'_{ij}(\boldsymbol{r})$ equal to $B_{ij}(\boldsymbol{r})$ inside the box $\Omega^{(e)}$ and 0 in the region outside the box $\Omega^{(e)}$ and inside the box $\Omega^{(c)}$ (sides $L_x^{(c)}$, $L_y^{(c)}$, $L_z^{(c)}$) that is larger than $\Omega^{(e)}$. Fourier transform of $B'_{ij}(\boldsymbol{r})$ on the box $\Omega^{(c)}$ is then defined as

$$B'_{ij}(\boldsymbol{r}) = \sum_{\boldsymbol{Q}\in \mathrm{inv}\Omega^{(c)}} B'_{ij}(\boldsymbol{Q}) e^{i\boldsymbol{Q}\cdot\boldsymbol{r}}. \tag{3.66}$$

The relation between the Fourier transforms of B_{ij} and B'_{ij} is given as

$$\begin{aligned} B'_{ij}(\boldsymbol{Q}) = \frac{1}{\Omega^{(c)}} \sum_{\boldsymbol{q}\in \mathrm{inv}\Omega^{(e)}} & B_{ij}(\boldsymbol{q}) I_0(-L_x^{(e)}/2, L_x^{(e)}/2, Q_x - q_x) \times \\ & \times I_0(-L_y^{(e)}/2, L_y^{(e)}/2, Q_y - q_y) I_0(-L_z^{(e)}/2, L_z^{(e)}/2, Q_z - q_z). \end{aligned} \tag{3.67}$$

where

$$I_0(a,b,k) = \int_a^b \mathrm{d}x e^{ikx} = \begin{cases} \frac{e^{ikb}-e^{ika}}{ik} & k \neq 0 \\ b-a & k = 0 \end{cases} \tag{3.68}$$

Eq. (3.59) can be recast as

$$V_{ijkl} = \int_{\Omega}^{(c)} \mathrm{d}^3\boldsymbol{r} \int_{\Omega}^{(c)} \mathrm{d}^3\boldsymbol{r}' B'_{ij}(\boldsymbol{r}) V(|\boldsymbol{r}-\boldsymbol{r}'|) B'_{kl}(\boldsymbol{r}'). \tag{3.69}$$

Applying the same procedure as in the derivation of Eq. (3.65), one obtains

$$V_{ijkl}^{(\mathrm{a1})} = \Omega^{(c)} \sum_{\substack{\boldsymbol{q}\in \mathrm{inv}\Omega^{(c)} \\ \boldsymbol{q}\neq 0}} B'_{ij}(\boldsymbol{q}) B'_{kl}(-\boldsymbol{q}) \frac{e^2}{\varepsilon q^2}. \tag{3.70}$$

Eq. (3.70) differs from Eq. (3.65) since a different approximation was used in its derivation. The integral over the region $\Omega^{(c)}$ was replaced by the integral over the whole space, which is a better approximation than the replacement of the integral over the region $\Omega^{(e)}$ in the derivation of Eq. (3.65), since the region $\Omega^{(c)}$ is larger than $\Omega^{(e)}$. Consequently, the error introduced by calculating V_{ijkl} using Eq. (3.70) now originates from the interactions among the charge $B_{ij}(\boldsymbol{r})$ of a single quantum dot and periodically replicated charges $B_{kl}(\boldsymbol{r})$ with periodicity defined by the box $\Omega^{(c)}$ rather than $\Omega^{(e)}$. Therefore, Eq. (3.70) can be systematically improved by an increase in $\Omega^{(c)}$, without increasing the number of plane waves needed to represent the wave functions.

We note that a similar philosophy can be used to remove the effects of strain field introduced by neighboring boxes. The reader interested in details of this procedure is referred to [89].

Another way to correct the error introduced by Coulomb interactions is to perform a multipole expansion of the difference between the Coulomb integral and its approximation given by Eq. (3.70), i.e. to perform the Makov-Payne correction. Such a procedure has been previously applied in ab initio [43] and empirical pseudopotential[24] calculations of aperiodic systems. The calculated value of the Coulomb integral can then be corrected by adding the first few terms (monopole, dipole and quadrupole) in the multipole expansion as

$$V_{ijkl}^{\mathrm{final}} = V_{ijkl}^{(\mathrm{a1})} - \frac{e^2}{4\pi\varepsilon}\left[q_{ij}q_{kl}a_{\mathrm{mad}} + \frac{4\pi}{3\Omega^{(c)}}\boldsymbol{d}_{ij}\cdot\boldsymbol{d}_{kl} - \frac{2\pi}{3\Omega^{(c)}}(q_{ij}Q_{kl}+q_{kl}Q_{ij})\right], \tag{3.71}$$

where

$$q_{ij} = \int_{\Omega^{(c)}} B'_{ij}(\boldsymbol{r})\mathrm{d}^3\boldsymbol{r} = \delta_{ij}, \tag{3.72}$$

$$\boldsymbol{d}_{ij} = \int_{\Omega^{(c)}} B'_{ij}(\boldsymbol{r})\boldsymbol{r}\,\mathrm{d}^3\boldsymbol{r}, \tag{3.73}$$

$$Q_{ij} = \int_{\Omega^{(c)}} B'_{ij}(\boldsymbol{r})r^2\mathrm{d}^3\boldsymbol{r}, \tag{3.74}$$

are the monopole, dipole and quadrupole terms respectively. The Madelung term a_{mad} is defined in terms of the Ewald sums and the self-interaction correction term as

$$a_{\mathrm{mad}} = \sum_{\substack{\boldsymbol{R}\in \mathrm{dir}\Omega^{(c)} \\ \boldsymbol{R}\neq 0}} \frac{\mathrm{erfc}(R\eta)}{R} + \frac{4\pi}{\Omega^{(c)}} \sum_{\substack{\boldsymbol{k}\in \mathrm{inv}\Omega^{(c)} \\ \boldsymbol{k}\neq 0}} \frac{\exp(-k^2/4\eta^2)}{k^2} - 2\frac{\eta}{\sqrt{\pi}} - \frac{\pi}{\eta^2 \Omega^{(c)}}.$$

The Ewald parameter η controls the rate of convergence of the sums. A reliable value that provides fast convergence is $\eta = \pi/\sqrt{L_x^{(c)} L_y^{(c)}}$.

Next, we illustrate the described methods for the correction of the Coulomb integral calculation by analyzing the dependence of the Coulomb integrals on $\Omega^{(c)}$ (dimensions $(L_x^{(c)}, L_y^{(c)}, L_z^{(c)})$). A set of calculations was done where $(m_x^{(c)}, m_y^{(c)}, m_z^{(c)})$ (used to determine the wave vector cutoff in Eq. (3.71)) was kept at a sufficiently large value of $(35, 35, 50)$ and the box dimensions were changed. Several direct Coulomb integrals $J_{ab} = V_{aabb}$ are shown in Fig. 3.4.

As seen from Fig. 3.4, the direct integrals without corrections calculated from Eq. (3.70) converge very slowly towards the numerically exact value obtained by performing the six dimensional integration in real space. For example, the box with dimension $(L_x^{(c)}, L_y^{(c)}, L_z^{(c)}) = (100, 100, 100)$ nm is sufficient only for precision of the order of 20 % and the box $(L_x^{(c)}, L_y^{(c)}, L_z^{(c)}) = (200, 200, 200)$ nm gives a precision of the order of 10 %. Following this procedure, numerically exact value can be approached within ∼3 % by reasonable systematical enlargement of the $V^{(c)}$ box. Further improvement in the accuracy of J_{ab} appears to be very difficult.

The results obtained by adding the monopole correction only in (3.71), are sufficient for the degree of accuracy one is usually interested in. The box $(L_x^{(c)}, L_y^{(c)}, L_z^{(c)}) = (60, 60, 60)$ nm is then sufficient for the precision of 1 % or better for the direct Coulomb integrals. The results with the three corrections involved are nearly indistinguishable from the numerically exact values for the direct Coulomb integrals. The box $(L_x^{(c)}, L_y^{(c)}, L_z^{(c)}) = (60, 60, 60)$ nm then already gives the precision better than 0.1 % for the values of direct integrals.

We illustrate the use of the methods developed by performing a full configuration interaction calculation of exciton and biexciton states. The rank of the configuration interaction matrix is

$$N_r^{\mathrm{CI}} = \binom{N_e}{n_e} \cdot \binom{N_h}{n_h} \tag{3.75}$$

where lowest N_e and topmost N_h states in conduction and valence band respectively form a basis of single-particle states for configuration interaction, while n_e and

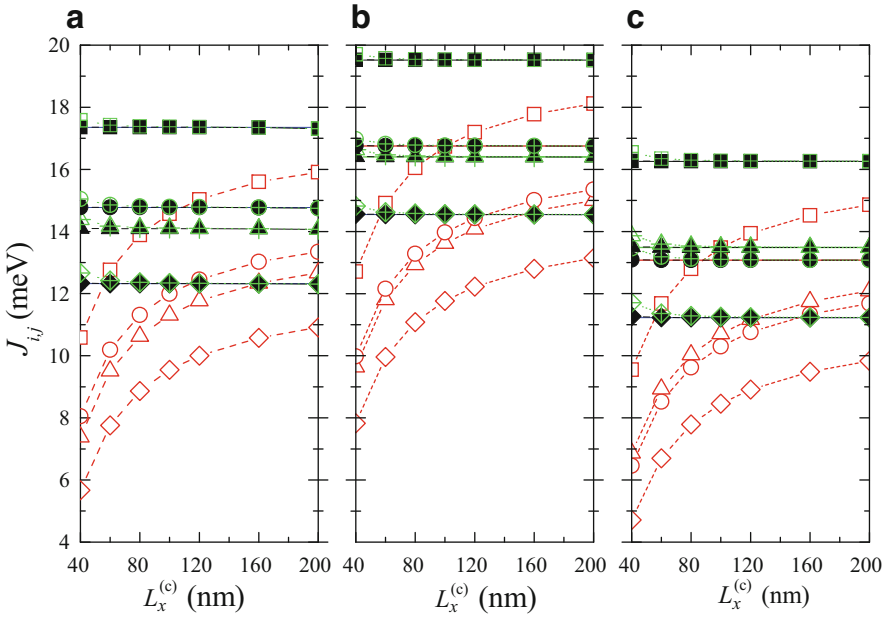

Fig. 3.4 The dependence of the values of Coulomb integrals in dot (**a**) of square-based truncated pyramidal shape with the bottom base width $b_b = 22\,\text{nm}$, the top base width $b_t = 5.5\,\text{nm}$, and the height $h = 4.425\,\text{nm}$, quantum dot (**b**) of truncated conical shape with the bottom base radius $R_b = 11\,\text{nm}$, the top base radius $R_t = 2.75\,\text{nm}$ and the height of $h = 4.425\,\text{nm}$, and quantum dot (**c**) in the shape of a lens with the radius $R = 15\,\text{nm}$ and the height $h = 4.425\,\text{nm}$ on the size of the embedding box dimension $L_x^{(c)}$. The calculation was done with $(m_x^{(c)}, m_y^{(c)}, m_z^{(c)}) = (35, 35, 50)$, $(L_x^{(c)}, L_y^{(c)}, L_z^{(c)}) = (L_x^{(c)}, L_x^{(c)}, L_x^{(c)})$. $J_{e0,h0}$ (*squares*), $J_{e1,h0}$ (*triangles*), $J_{e0,h1}$ (*circles*), and $J_{e1,h1}$ (*diamonds*). The results without corrections (*open symbols*), the results with the monopole correction only (*open symbols with cross*), and the results with monopole, dipole and quadrupole correction (*solid symbols*) are shown. The results obtained by real space integration are indistinguishable from the results obtained by including the three corrections

n_h are the number of electrons and holes that form the many-body complex. The number of Coulomb integrals needed to construct the configuration Hamiltonian is $(N_e + N_h)^4$. By exploiting the relations $V_{jilk} = V^*_{ijkl}$ and $V_{lkji} = V^*_{ijkl}$, the whole problem can be reduced to the calculation of $[(N_e + N_h)(N_e + N_h + 1)/2]^2$ integrals. Additionally, symmetry considerations imply that only Coulomb integrals V_{ijkl} whose wave functions satisfy the conservation of the total quasi-angular momentum:

$$\{m_j + m_l \equiv m_i + m_k \pmod 2\} \tag{3.76}$$

are nonzero. This additionally reduces the number of integrals that need to be calculated by a factor of 2. In our case, all 354,025 Coulomb integrals among the states from the set including first $N_e = 14$ electron and first $N_h = 20$ states were calculated. The calculation of such a big number of Coulomb integrals is performed efficiently by exploiting the following two facts: (1) $B_{ij}(\boldsymbol{q})$, (3.63), that enters the expression for Coulomb integrals, (3.70), via (3.67) and the expressions for multipole corrections (3.72), (3.73), (3.74), needs to be calculated just $(N_e + N_h)(N_e + N_h + 1)/2$ times; (2) summation in (3.67) over vectors $\boldsymbol{q}$, which should be in principle done in the domain $|n_{\boldsymbol{r}}| \leq 2m_{\boldsymbol{r}}^{(e)}$, can be done in the reduced domain $|n_{\boldsymbol{r}}| \leq m_{\boldsymbol{r}}^{(e)}$, since the relative error introduced in V_{ijkl} by this truncation is $< 10^{-5}$. One should also note that when a particular set of Coulomb integrals is calculated, it can be used for configuration interaction calculations with different values of n_e and n_h, without the need of recalculating the integrals.

In order to determine the number of single-particle states sufficient for the use in configuration interaction expansion, two sets of calculations were performed. In the first set, the number of hole states was set to $N_h = 20$ and N_e was varied. In the second set, the number of electron states was set to $N_e = 14$ and N_h was varied. The results are shown in Fig. 3.5. One can estimate from the results presented in Fig. 3.5 that $N_e = 10$ is sufficient for convergence of exciton ground state of the order of 0.2 meV and biexciton ground state of the order of 0.5 meV. For the same degree of precision, a larger number of hole states $N_h = 14$ is needed, as a consequence of smaller energy difference among hole single particle states.

3.9 Symmetries of Single Particle States in Quantum Dots

In this section, we show first how one can exploit the symmetry to block diagonalize the Hamiltonian matrix, which leads to a more efficient solution of its eigenvalue problem. Then we show how one can identify the symmetry group of the Hamiltonian and analyze the symmetries of various Hamiltonians that describe the same physical system.

Symmetry-based block diagonalization of the quantum dot **k·p** Hamiltonian matrix was performed for the first time in [88] and [87], for the cases of fourfold and sixfold symmetry respectively. The same approach can be extended to M-fold symmetry. Block diagonalization is achieved by representing the Hamiltonian in the so called symmetry adapted basis. If we denote the plane wave basis state where the envelope function of band b is equal to $a_{\boldsymbol{k}}(\boldsymbol{r})$ and the other envelope functions are zero as $|\boldsymbol{k}, b\rangle$, This is done by state where the envelope function of band b is equal to $a_{\boldsymbol{k}}(\boldsymbol{r})$ and the other envelope functions are zero) to the basis of the states characterized by a given value of the z-component of the total quasi-angular momentum m_f. In the case of M-fold symmetry, this basis is composed of the

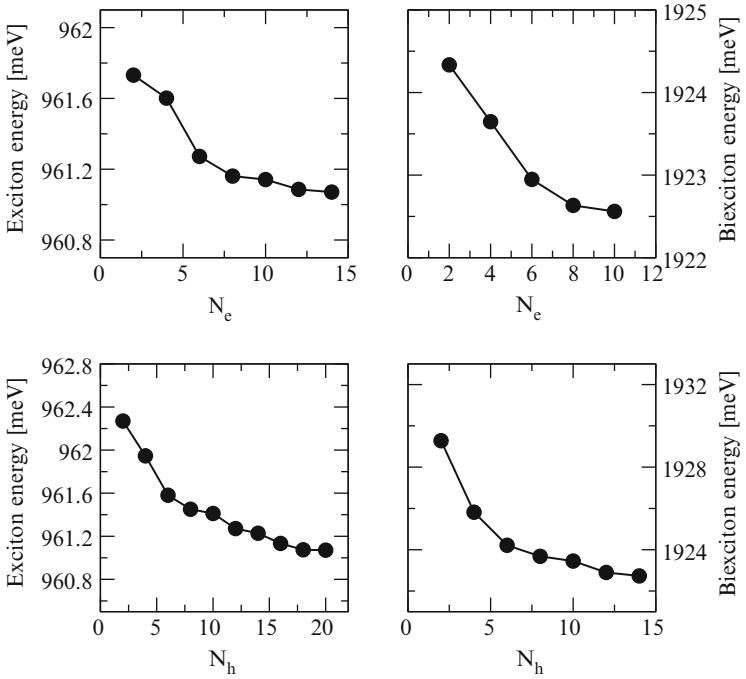

Fig. 3.5 The dependence of exciton and biexciton energy in quantum dot (a) from Fig. 3.4 on the number of electron N_e states (when $N_h = 20$) and hole N_h (when $N_e = 14$) states used for configuration interaction expansion

following elements the vectors of the symmetry adapted basis in the case of the system with M-fold symmetry are given as

$$|A_{m_f}, \boldsymbol{k}, b\rangle = \frac{1}{\sqrt{M}} \sum_{l=0}^{M-1} e^{il\phi(m_f - J_z(b))} |R_{l\phi}\boldsymbol{k}, b\rangle \tag{3.77}$$

with $\boldsymbol{k}$-vectors satisfying $k_x^2 + k_y^2 > 0$ and $0 \leq k_y < \tan(\phi)k_x$,

$$|A_{m_f}, \boldsymbol{k}, b\rangle = |\boldsymbol{k}, b\rangle \tag{3.78}$$

with $\boldsymbol{k}$-vectors satisfying $k_x = k_y = 0$ and the band b satisfying $(J_z(b) - m_f)\text{mod } M = 0$. In previous equations $\phi = 2\pi/M$, $J_z(b)$ is the z-component of the total quasi-angular momentum of the Bloch function of band b, $R_{l\phi}\boldsymbol{k} = \boldsymbol{k}'$ is the vector obtained by rotation of the vector $\boldsymbol{k}$ by an angle $l\phi$ around the z-axis

$$\begin{aligned} k_x' + ik_y' &= e^{il\phi}(k_x + ik_y), \\ k_z' &= k_z. \end{aligned} \tag{3.79}$$

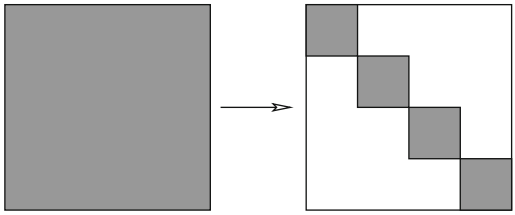

Fig. 3.6 The scheme of the Hamiltonian matrix in the plane wave basis (*left*) and in the symmetry adapted basis (*right*)

The quasi-angular momentum of the basis state m_f takes the values from the interval $[-(M-1)/2, (M-1)/2]$ with a step of 1. In the symmetry adapted basis, the Hamiltonian matrix elements are nonzero between basis states with the same m_f only. As a consequence, the Hamiltonian matrix is block diagonal (see Fig. 3.6); it is composed of M smaller matrices of approximately equal size. Since diagonalization cost of the Hamiltonian matrix is proportional to N_r^3 (where N_r is the rank of the matrix), the total cost of the diagonalization is then $\propto M \times (N_r/M)^3$, which is M^2 times faster than if symmetry were not used.

The symmetry of the Hamiltonian is not necessarily equal to the symmetry of the system. In fact, there has been a belief that $\mathbf{k} \cdot \mathbf{p}$ Hamiltonians predict a higher symmetry than the true symmetry of the system. In what follows, we analyze the square based pyramidal quantum dot with base width to height ratio $b/h = 2$ modeled with different $\mathbf{k} \cdot \mathbf{p}$ Hamiltonians. We consider the following Hamiltonians:

(a) The 8-band $\mathbf{k} \cdot \mathbf{p}$ Hamiltonian consisting of kinetic part only [without spin-orbit interaction and strain].
(b) The 8-band $\mathbf{k} \cdot \mathbf{p}$ Hamiltonian consisting of kinetic part with spin-orbit interaction taken into account [but without strain].
(c) The 8-band $\mathbf{k} \cdot \mathbf{p}$ Hamiltonian consisting of kinetic part with interface band-mixing effects taken into account [but without spin-orbit interaction and strain].
(d) The standard 8-band $\mathbf{k} \cdot \mathbf{p}$ Hamiltonian consisting of kinetic part with spin-orbit interaction and strain, as well as the strain-induced piezoelectric potential. It was assumed that piezoelectric polarization depends linearly on strain.
(e) The 8-band $\mathbf{k} \cdot \mathbf{p}$ Hamiltonian consisting of kinetic part with spin-orbit interaction and strain, as well as the strain-induced piezoelectric potential and the interface Hamiltonian.
(f) The 14-band $\mathbf{k} \cdot \mathbf{p}$ Hamiltonian consisting of the kinetic part only [without spin-orbit interaction and strain].

In what follows, we will refer to each of these Hamiltonians as models (a)-(f). We show that the inclusion of additional bands in the Hamiltonian or the inclusion of interface effects lead to the true symmetry of the system.

We start our considerations with model (a). The symmetry group of such a model applied to a pyramidal square-based quantum dot is the C_{4v} group, as demonstrated

Table 3.2 Energies (in eV) of top six hole energy levels and bottom four electron levels, for a square-based pyramidal InAs/GaAs quantum dot with base width $b = 100$ Å, and base to height ratio $b/h = 2$ calculated using different models

State	(a)	(b)	(c)	(d)	(e)	(f)
e3	1.08163	1.06674	1.08878	1.30684	1.30772	1.03852
e2	0.99336	0.96795	1.00170	1.25044	1.25570	0.97301
e1	0.99336	0.96724	1.00074	1.23439	1.23943	0.97298
e0	0.84346	0.81808	0.85115	1.12013	1.12543	0.83509
h0	−0.06722	−0.03427	−0.06475	−0.05230	−0.05052	−0.06512
h1	−0.06722	−0.03680	−0.06698	−0.06827	−0.06699	−0.06517
h2	−0.07389	−0.03765	−0.07248	−0.07840	−0.07843	−0.07263
h3	−0.07883	−0.04244	−0.07708	−0.09115	−0.09046	−0.07700
h4	−0.08518	−0.04582	−0.08119	−0.10517	−0.10565	−0.08124
h5	−0.08518	−0.04614	−0.08360	−0.10888	−0.10859	−0.08270

The letters in the first row in the table specify the model used in the calculation

in Sect. 3.5. We discuss the signatures of symmetry of the model (a) in the energy level structure [given in Table 3.2(a)] and the shape of the wavefunctions [presented in Fig. 3.7(a)]. Several pairs of energy levels [(e_1,e_2), (h_0,h_1) and (h_4,h_5)] are degenerate as a consequence of the fact that the C_{4v} group has a two dimensional representation E (the notation of [10]). The states that transform according to this representation therefore come in pairs and are degenerate. The wave function probability density isosurfaces also reflect the high symmetry of the system—they all have a perfectly C_{4v} symmetric shape.

Next, we include spin-orbit interaction in model (a) and get model (b). The eigenstates of the Hamiltonian of such a model transform according to a representation of the double C_{4v} group which is a direct product of the representation of the single C_{4v} group and the representation $\mathscr{D}_{1/2}$ according to which the spin functions transform ([10], p. 142). When the representation obtained from the direct product is reducible, the inclusion of spin-orbit interaction leads to the removal of degeneracy of energy levels. Indeed, the product $E \times \mathscr{D}_{1/2}$ is equal to $E_1' + E_2'$ (the notation of [10]). While, it is well understood that the effect of spin-orbit interaction on the states in the valence band is rather strong, we would like to point out a less known fact that the spin-orbit interaction also causes the splitting of the e_1 and e_2 states [shown in Table 3.2(b)]. The existence of this splitting was established in [88] for pyramidal quantum dots and later on analyzed again in [20] for lens-shaped quantum dots. It is important to note here that symmetry reduction is not the cause of this energy level splitting effect. Indeed, one can see in Fig. 3.7b that the probability density isosurfaces exhibit a perfect C_{4v} symmetry.

To understand the effect of interface terms in the Hamiltonian on the symmetry of the model, we analyze model (c). One can derive analytically that the [001] interface term leads to the reduction of symmetry from C_{4v} to C_{2v} (see Sect. 3.4). Similar

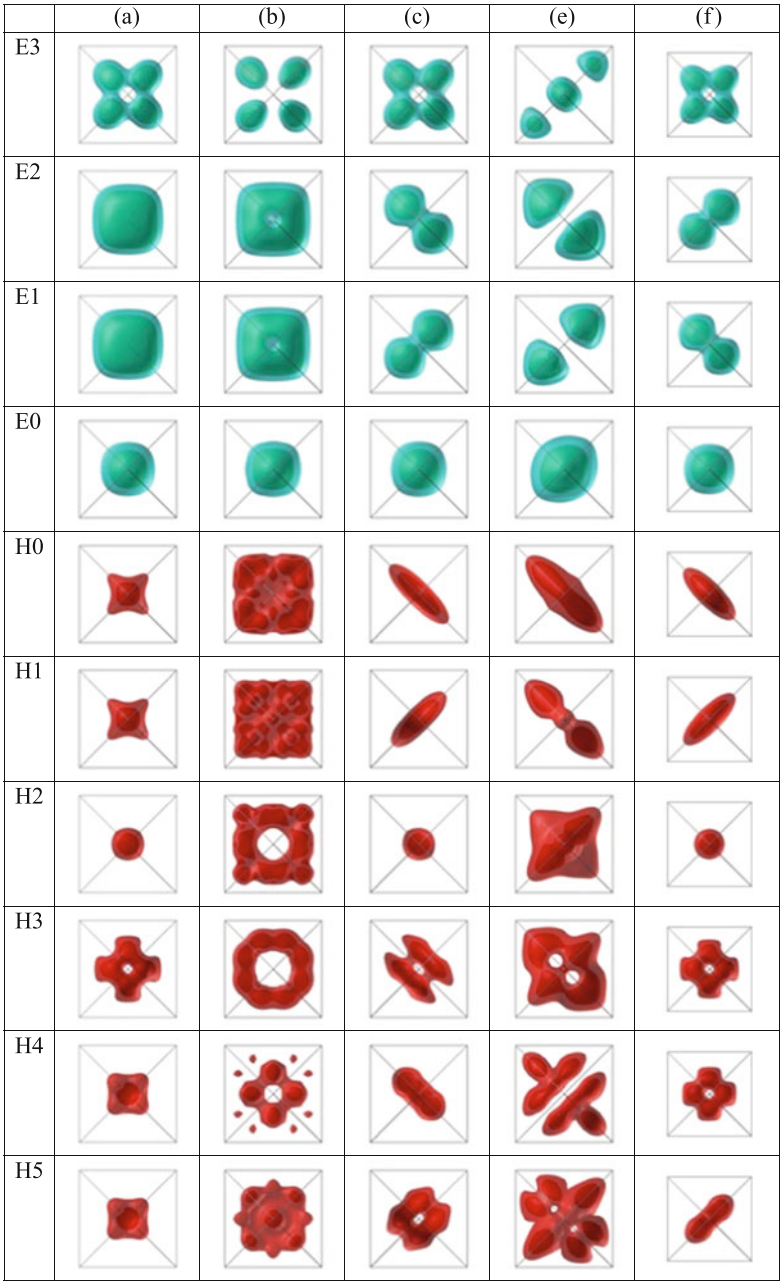

Fig. 3.7 The wavefunctions squared for top six hole states and bottom five electron states for a square-based pyramidal InAs/GaAs quantum dot with base width $b = 100$ Å, and base to height ratio $b/h = 2$ calculated using different models. The letters (a)–(c), (e)–(f) specify the model used in the calculation. The isosurfaces are plotted at 25 % (transparent) and 75 % of the maximal charge density

derivations also show that the joint effect of other four interfaces leads to the same symmetry reduction. Since the C_{2v} group has one dimensional irreducible representations only, no double degenerate eigenstates can be present. Consequently, the effect of interfaces leads to splitting of degenerate states by typically 1–3 meV, as shown in Table 3.2(c). The shapes of the wave function moduli isosurfaces also reduce their symmetry from C_{4v} [Fig. 3.7(a)] to C_{2v} [Fig. 3.7(c)].

Model (f) that also includes the second conduction band is considered next. Analytical derivations (Sect. 3.5) show that the inclusion of the additional bands also leads to reduction of symmetry to C_{2v}. The terms that contain the P_2 element which couples the top of the valence band, Γ_{5v}, [that originates from the p bonding states (denoted as p_b) of atoms in the bulk] with the second conduction band, Γ_{5c}, [that originates from the p antibonding states (denoted as p_a) of atoms in the bulk] are the only terms that prevent the C_{4v} symmetry. Therefore the P_2 element can be identified as the symmetry breaking term in model (f). This term introduces the splittings, Table 3.2(f), which are less pronounced than these of the interface terms—for example the splitting of e_1 and e_2 is less than 0.1 meV. The effect of this symmetry breaking on the wave functions is generally similar [see Fig. 3.7(f)] as in the case of interface-induced symmetry breaking.

Analytical derivations and the numerical results presented therefore indicate that the inclusion of bands beyond the standard 8 bands, as well as the inclusion of interface effects within the $\mathbf{k}\cdot\mathbf{p}$ approach both lead to a correct description of the symmetry of the system. As a consequence, a widespread belief that $\mathbf{k}\cdot\mathbf{p}$ Hamiltonians are not capable to capture the correct symmetry of the system appears not to be correct.

It has been previously well known [88] that the piezoelectric effect also reduces the symmetry from C_{4v} to C_{2v}. The results shown in Table 3.2 (d), (e) indicate that splitting of e_1 and e_2 states induced by the piezoelectric effect is stronger than the splittings induced by other effects. One should also stress that in the absence of piezoelectric effect, the strain would also give rise to symmetry reduction if it were modeled using the Valence force field model [9, 57, 75, 76, 78]

3.10 Symmetries of Exciton States in Quantum Dots

In this section, we discuss the signatures of symmetry in the exciton spectra and in the optical properties of excitons. We identify the changes in the spectrum when spin-orbit interaction is taken into account and when symmetry group of the model is lowered from C_{4v} to C_{2v}.

We start by considering model (a) of the previous section. In such a model, the single particle states transform according to single valued irreducible representations (IRs) of the C_{4v} group. We find that the h_0 state transforms according to two dimensional representation E, while the e_0 state transforms as A_1 representation

(the notation of [19]). Therefore, h_0 is fourfold degenerate (including the twofold spin degeneracy), while e_0 is twofold degenerate.

Exciton states transform according to single values IRs of the symmetry group [84]. The IRs of the exciton states in the ground exciton manifold can be obtained from the direct product of the IR of the e_0 state and complex conjugated IR of the h_0 state. In model (a) this gives $A_1 \times E = E$. Therefore, the orbital part of the exciton state transform as E. In addition, the spins of an electron and a hole that form an exciton can form either the singlet or the triplet state. As a consequence, the ground eight-dimensional manifold consists of the doubly degenerate ground state (that originates from the E symmetry of the orbital part and the singlet of the spin part) and sixfold degenerate excited state (stemming from the E symmetry of the orbital part and the triplet of the spin part). An E exciton is allowed to emit xy-polarized radiation, while it is not allowed to emit z-polarized radiation. On the other hand, due to conservation of spin in the optical transition, the singlet state is dark, while in the triplet two states are bright and one is dark. This implies that the twofold-degenerate ground exciton state is dark while the sixfold degenerate excited state consists of four bright and two dark states.

Next, we discuss the changes in the spectrum when spin-orbit interaction is included as in model (b) of the previous section. In model (b) the single particle states transform according to double valued IRs of the C_{4v} group. We find that the h_0 state transforms as $\overline{E}_2$, while the e_0 state transforms as $\overline{E}_1$. Both of them are twofold degenerate. The IRs of states in the four dimensional exciton manifold are then obtained from $\overline{E}_1 \times \overline{E}_2 = E + B_1 + B_2$. Therefore, the ground exciton manifold consists of a doubly degenerate E exciton and non-degenerate B_1 and B_2 excitons. The E exciton is allowed to emit xy-polarized radiation, while B_1 and B_2 excitons are dark. Among higher excited exciton states, the states that transforms as B_1, B_2 and A_2 are non-degenerate and dark, the states that transform as A_1 are non-degenerate and emit z-polarized radiation, while the states that transform as E are double-degenerate and emit xy-polarized radiation.

The effects that arise when the symmetry is lowered from C_{4v} to C_{2v}, as for example in models (c) and (f) (that exclude spin-orbit interaction) in the previous section, are discussed next. The subduction of the IR E of the C_{4v} group to the IRs of the C_{2v} group yields $E \rightarrow B_1 + B_2$. Therefore, the h_0 state that transformed as E in model (a), transforms now as either B_1 or B_2. The e_0 state still transforms as A_1. As a consequence, both e_0 and h_0 are two fold degenerate (including the twofold spin degeneracy). The ground exciton manifold is now four dimensional. The orbital part of the exciton states in ground exciton manifold transforms as B_1 or B_2 (depending whether h_0 transforms as B_1 or B_2). As a consequence, the ground exciton manifold consists of the non-degenerate ground state (that originates from the singlet of the spin part and is dark) and the threefold degenerate excited states (that originate from the triplet of the spin part). Two of these excited states are bright and can emit xy-polarized radiation, while one is dark.

Finally we discuss the symmetry lowering effects in models (c) or (d) (that include spin-orbit interaction). The subductions of the IRs $\overline{E}_1$ and $\overline{E}_2$ of the C_{4v}

group to the C_{2v} group yield $\overline{E}_1 \rightarrow \overline{E}$ and $\overline{E}_2 \rightarrow \overline{E}$. As a consequence, both h_0 and e_0 now transform as $\overline{E}$. The IRs of the states in the four dimensional ground exciton manifold then stem from $\overline{E} \times \overline{E} = A_1 + A_2 + B_1 + B_2$. The B_1 and B_2 states originate from the E state in the model with C_{4v} symmetry. Therefore, lowering of symmetry from C_{4v} to C_{2v} splits the E exciton into two non-degenerate B_1 and B_2 excitons. B_1 and B_2 inherit the brightness from the E exciton. The A_2 state originates from the B_2 state in the model with C_{4v} symmetry. It remains non-degenerate and dark. On the other hand, the A_1 state originates from the dark B_1 state in the model with C_{4v} symmetry. It remains non-degenerate but the A_1 state is bright and is allowed to emit z-polarized radiation. However, one should note that the bright state that originates from the dark state of the higher symmetry group is typically only weakly bright as we have verified by numerical calculations of the dipole matrix elements that correspond to such states. Among higher excited exciton states, the states that transforms as A_2 are dark, the states that transform as A_1 emit z-polarized radiation, while the states that transform as B_1 or B_2 emit xy-polarized radiation.

3.11 Conclusion

In this chapter, we have demonstrated the importance of understanding the symmetry of the $\mathbf{k} \cdot \mathbf{p}$ Hamiltonians used in electronic structure calculations. On this route, the interface term which is rarely considered was derived first, as it is essential for capturing the proper symmetry of the system. The plane wave method introduces an artificial translational symmetry accompanied by artificial Coulomb interaction between the carrier in the dot and its periodic replicas. Artifacts of this interaction can be removed by a careful modification of the procedure for calculation of Coulomb integrals. We show how one can identify the symmetry group of a certain $\mathbf{k} \cdot \mathbf{p}$ Hamiltonian. An example of a square-based pyramidal quantum dot is then used to show how the symmetry changes with the change in the level of sophistication of the model. The standard 8-band $\mathbf{k} \cdot \mathbf{p}$ Hamiltonian exhibits an artificially high C_{4v} symmetry. However, both the inclusion of the effect of interfaces and the inclusion of additional bands in the model lead to correct C_{2v} symmetry. Once the symmetry of the Hamiltonian is understood, it can be used to choose the basis in which the Hamiltonian is block diagonal and consequently largely reduce the computational effort.

Acknowledgements Stanko Tomić* wishes to thank to the STFC e-Science, UK, for providing the computational resources, and the Royal Society, London, Research Grant "High Performance Computing in Modelling of Innovative High Efficiency Photovoltaic Devices". Nenad Vukmirović was supported by European Community FP7 Marie Curie Career Integration Grant (ELECTROMAT), Serbian Ministry of Education, Science and Technological Development (project ON171017) and FP7 projects PRACE-2IP, PRACE-3IP, HP-SEE, and EGI-InSPIRE.

Appendix

The values of the relevant material parameters appearing in the kp-Hamiltonians are given in Table 3.3.

Table 3.3 Relevant material parameters of binary compound semiconductors GaAs, InAs, and AlAs

	GaAs	InAs	AlAs
a_0 [Å]	5.6503	6.0553	5.661
α [meV/K]	0.5405	0.276	0.885
β [K]	204	93	530
$E_{g0} = E(\Gamma_{1c}) - E(\Gamma_{5v})$ [eV]	1.518	0.405	3.099
$E_{g1} = E(\Gamma_{5c}) - E(\Gamma_{5v})$ [eV]	4.488	4.38	4.54
$E_{g2} = E(\Gamma_{5v}) - E(\Gamma_{1v})$ [eV]	12.50	12.64	11.95
E_{P0} [eV]	25.7	21.846	21.1
E_{P1} [eV]	0.19	0.03	0.16
E_{P2} [eV]	14.79	19.0	16.8
E_{P3} [eV]	2.3	0.6	0.1
E_{P4} [eV]	0.2	2.55	0.0 (n/a)
$E_{v,av}$ [eV]	−6.920	−6.747	−7.49
m_c^*	0.0667	0.02226	0.15
$\Delta_{\mathrm{so}}(p_a)$[eV]	0.340	0.380	0.280
$\Delta_{\mathrm{so}}(p_b)$[eV]	0.170	0.190	0.150
Δ_{cf}[eV]	0.085	0.085	0.085
c_{11} [GPa]	118.8	83.3	125.0
c_{12} [GPa]	53.8	45.3	53.4
c_{44} [GPa]	59.4	39.6	54.2
a_c [eV]	−8.013	−5.08	−5.64
a_v [eV]	0.220	1.00	2.47
b_{ax} [eV]	−1.824	−1.800	−2.3
d_{ax} [eV]	−5.062	−3.600	−3.4
e_{14} [C m^{-2}]	0.160	0.045	0.225
$\gamma_1^L, \gamma_2^L, \gamma_3^L$	7.10, 2.02, 2.91	19.67, 8.40, 9.30	3.76, 0.82, 1.42
ϵ_r	13.18	14.6	10.1

a_0 are the lattice constants, α and β are the Varshni parameters that describe the temperature dependence of the band gap (a temperature of 4K was assumed in all calculations), E_{gi} are the band gaps, E_{Pi} are the energies related to interband matrix elements of the velocity operator P_i as $E_{Pi} = 2m_0 P_i^2/\hbar^2$, $E_{v,av}$ is the average valence band edge energy at the Γ point, m_c^* is the conduction band effective mass. $\Delta_{\mathrm{so}}(p_a)$ is the spin-orbit splitting in the second conduction band, $\Delta_{\mathrm{so}}(p_b)$ is the spin-orbit splitting in the valence band and Δ_{cf} the crystal field splitting. c_{ij} are the elastic constants. a_c, a_v, b_{ax}, d_{ax} are the deformation potentials, e_{14} is the piezoelectric constant. $\gamma_1^L, \gamma_2^L, \gamma_3^L$ are the Luttinger parameters in the 6-band model. ϵ_r is the static dielectric constant

References

1. N. Akopian, N.H. Lindner, E. Poem, Y. Berlatzky, J. Avron, D. Gershoni, B.D. Gerardot, P.M. Petroff, Entangled photon pairs from semiconductor quantum dots. Phys. Rev. Lett. **96**, 130–501 (2006)
2. A.P. Alivisatos, W.W. Gu, C. Larabell, Quantum dots as cellular probes. Ann. Rev. Biomed. Eng. **7**, 55–76 (2005)
3. A.D. Andreev, Conference on In-Plane Semiconductor Lasers - From Ultraviolet to Mid-Infrared II, San Jose, CA, Jan 26–28, 1998, pp 151–161
4. A.D. Andreev, J.R. Downes, D.A. Faux, E.P. O'Reilly, Strain distributions in quantum dots of arbitrary shape. J. Appl. Phys. **86**, 297–305 (1999)
5. A.D. Andreev, E.P. O'Reilly, Theory of the electronic structure of GaN/AlN hexagonal quantum dots. Phys. Rev. B **62**, 15,851–15,870 (2000)
6. C.G. Bailey, D.V. Forbes, R.P. Raffaelle, S.M. Hubbard, Near 1 v open circuit voltage InAs/GaAs quantum dot solar cells. Appl. Phys. Lett. **98**(16), 163105 (2011)
7. G.A. Baraff, D. Gershoni, Eigenfunction-expansion method for solving the quantum-wire problem: Formulation. Phys. Rev. B **43**, 4011–4022 (1991)
8. P. Bhattacharya, S. Ghosh, A.D. Stiff-Roberts, Quantum dot opto-electronic devices. Ann. Rev. Mat. Res. **34**, 1–40 (2004)
9. D. Bimberg, M. Grundmann, N.N. Ledentsov, *Quantum dot heterostructures* (John Wiley, Chichester, 1999)
10. G.L. Bir, G.E. Pikus, *Symmetry and strain-induced effects in semiconductors* (Wiley, New York, 1974)
11. S. Blokhin, A. Sakharov, A. Nadtochy, A. Pauysov, M. Maximov, N. Ledentsov, A. Kovsh, S. Mikhrin, V. Lantratov, S. Mintairov, N. Kaluzhniy, M. Shvarts, AlGaAs/GaAs photovoltaic cells with an array of InGaAs qds. Semiconductors **43**, 514–518 (2009)
12. C. Bulutay, Pseudopotential-based full zone $\mathbf{k}\cdot\mathbf{p}$ technique for indirect bandgap semiconductors: Si, Ge, diamond and Sic. Turk. J. Phys. **30**, 287–294 (2006)
13. M.G. Burt, The justification for applying the effective-mass approximation to microstructures. J. Phys.: Condens. Matter **4**, 6651–6690 (1992)
14. M. Cardona, N.E. Christensen, G. Fasol, Relativistic band structure and spin-orbit splitting of zinc-blende-type semiconductors. Phys. Rev. B **38**(3), 1806–1827 (1988)
15. M. Cardona, F.H. Pollak, Energy-band structure of germanium and silicon: The $\mathbf{k}\cdot\mathbf{p}$ method. Phys. Rev. **142**(2), 530–543 (1966)
16. M.A. Cusack, P.R. Briddon, M. Jaros, Electronic structure of InAs/GaAs self-assembled quantum dots. Phys. Rev. B **54**, R2300–R2303 (1996)
17. J.P. Cuypers, W. van Haeringen, Coupling between γ- and x-type envelope functions at GaAs/Al(Ga)As interfaces. Phys. Rev. B **48**(15), 11,469–11,472 (1993)
18. K. Eichkorn, R. Ahlrichs, Cadmium selenide semiconductor nanocrystals: a theoretical study. Chem. Phys. Lett. **288**, 235–242 (1998)
19. J.P. Elliott, P.G. Dawber, *Symmetry in Physics* (Macmillan, London, 1979)
20. J. Even, F. Doré, C. Cornet, L. Pedesseau, Semianalytical model for simulation of electronic properties of narrow-gap strained semiconductor quantum nanostructures. Phys. Rev. B **77**, 085305 (2008)
21. B.A. Foreman, Analytical envelope-function theory of interface band mixing. Phys. Rev. Lett. **81**(2), 425–428 (1998)
22. B.A. Foreman, Analytical envelope-function theory of interface band mixing. Phys. Rev. Lett. **81**, 425–428 (1998)
23. N. Fraj, I. Saïdi, S.B. Radhia, K. Boujdaria, Band structures of AlAs, gap, and SiGe alloys: A 30 $\mathbf{k}\cdot\mathbf{p}$ model. J. Appl. Phys. **102**(5), 053703 (2007)
24. A. Franceschetti, H. Fu, L.W. Wang, A. Zunger, Many-body pseudopotential theory of excitons in inp and cdse quantum dots. Phys. Rev. B **60**, 1819–1829 (1999)

25. C.S. Garoufalis, A.D. Zdetsis, S. Grimme, High level ab initio calculations of the optical gap of small silicon quantum dots. Phys. Rev. Lett. **87**, 276,402 (2001)
26. D. Gershoni, C.H. Henry, G.A. Baraff, Calculating the optical properties of multidimensional heterostructures: Application to the modeling of quaternary quantum well lasers. IEEE J. Quantum Electron. **29**, 2433–2450 (1993)
27. C. Hermann, C. Weisbuch, $\mathbf{k}\cdot\mathbf{p}$ perturbation theory in iii-v compounds and alloys: a reexamination. Phys. Rev. B **15**(2), 823–833 (1977)
28. S.M. Hubbard, C.D. Cress, C.G. Bailey, R.P. Raffaelle, S.G. Bailey, D.M. Wilt, Effect of strain compensation on quantum dot enhanced GaAs solar cells. Appl. Phys. Lett. **92**(12), 123512 (2008)
29. H. Jiang, J. Singh, Strain distribution and electronic spectra of InAs/GaAs self-assembled dots: An eight-band study. Phys. Rev. B **56**, 4696–4701 (1997)
30. J. Kim, L.W. Wang, A. Zunger, Comparison of the electronic structure of InAs/GaAs pyramidal quantum dots with different facet orientations. Phys. Rev. B **57**(16), R9408–R9411 (1998)
31. N. Kirstaedter, N.N. Ledentsov, M. Grundmann, D. Bimberg, V.M. Ustinov, S.S. Ruvimov, M.V. Maximov, P.S. Kopev, Z.I. Alferov, U. Richter, P. Werner, U. Gosele, J. Heydenreich, Low-threshold, large T_0 injection-laser emission from (InGa)As quantum dots. Electron. Lett. **30**, 1416–1417 (1994)
32. P.C. Klipstein, Operator ordering and interface-band mixing in the Kane-like Hamiltonian of lattice-matched semiconductor superlattices with abrupt interfaces. Phys. Rev. B **81**(23), 235–314 (2010)
33. M.E. Kurdi, G. Fishman, S. Sauvage, P. Boucaud, Band structure and optical gain of tensile-strained germanium based on a 30 band $\mathbf{k}\cdot\mathbf{p}$ formalism. J. Appl. Phys. **107**(1), 013710 (2010)
34. O.L. Lazarenkova, A.A. Balandin, Miniband formation in a quantum dot crystal. J. Appl. Phys. **89**(10), 5509–5515 (2001)
35. S. Lee, J. Kim, L. Jönsson, J.W. Wilkins, G.W. Bryant, G. Klimeck, Many-body levels of optically excited and multiply charged InAs nanocrystals modeled by semiempirical tight binding. Phys. Rev. B **66**, 235,307 (2002)
36. J. Li, L.W. Wang, Energy levels of isoelectronic impurities by large scale LDA calculations. Phys. Rev. B **67**, 033,102 (2003)
37. J. Li, L.W. Wang, First principles calculations of ZnS:Te energy levels. Phys. Rev. B **67**, 205,319 (2003)
38. J. Li, L.W. Wang, Band-structure-corrected local density approximation study of semiconductor quantum dots and wires. Phys. Rev. B **72**, 125325 (2005)
39. S.S. Li, J.B. Xia, Z.L. Yuan, Z.Y. Xu, W. Ge, X.R. Wang, Y. Wang, J. Wang, L.L. Chang, Effective-mass theory for InAs/GaAs strained coupled quantum dots. Phys. Rev. B **54**, 11,575–11,581 (1996)
40. J.M. Luttinger, Quantum theory of cyclotron resonance in semiconductors: general theory. Phys. Rev. **102**, 1030–1041 (1956)
41. J.M. Luttinger, W. Kohn, Motion of electrons and holes in perturbed periodic fields. Phys. Rev. **97**, 869–883 (1955)
42. S. Maimon, E. Finkman, G. Bahir, S.E. Schacham, J.M. Garcia, P.M. Petroff, Intersublevel transitions in InAs/GaAs quantum dots infrared photodetectors. Appl. Phys. Lett. **73**, 2003–2005 (1998)
43. G. Makov, M.C. Payne, Periodic boundary conditions in *ab initio* calculations. Phys. Rev. B **51**, 4014–4022 (1995)
44. H. Mayer, U. Rössler, Spin splitting and anisotropy of cyclotron resonance in the conduction band of GaAs. Phys. Rev. B **44**(16), 9048–9051 (1991)
45. P. Michler, A. Kiraz, C. Becher, W.V. Schoenfeld, P.M. Petroff, L.D. Zhang, E. Hu, A. Imamoglu, A quantum dot single-photon turnstile device. Science **290**, 2282 (2000)
46. V. Mlinar, M. Tadić, F.M. Peeters, Hole and exciton energy levels in InP/$\mathrm{In}_x\mathrm{Ga}_{1-x}$P quantum dot molecules: Influence of geometry and magnetic field dependence. Phys. Rev. B **73**, 235,336 (2006)

47. T. Nakaoka, T. Saito, J. Tatebayashi, Y. Arakawa, Size, shape and strain dependence of the g factor in self-assembled In(Ga)As quantum dots. Phys. Rev. B **70**, 235,337 (2004)
48. A. Nozik, Quantum dot solar cells. Physica E **14**(1-2), 115–120 (2002)
49. R. Oshima, A. Takata, Y. Okada, Strain-compensated InAs/GaNAs quantum dots for use in high-efficiency solar cells. Appl. Phys. Lett. **93**(8), 083111 (2008)
50. D. Pan, E. Towe, S. Kennerly, Normal-incidence intersubband (In,Ga)As/GaAs quantum dot infrared photodetectors. Appl. Phys. Lett. **73**, 1937–1939 (1998)
51. D. Pan, Y.P. Zeng, M.Y. Kong, J. Wu, Y.Q. Zhu, C.H. Zhang, J.M. Li, C.Y. Wang, Normal incident infrared absorption from InGaAs/GaAs quantum dot superlattice. Electron. Lett. **32**, 1726–1727 (1996)
52. P.M. Petroff, S.P. DenBaars, MBE and MOCVD growth and Properties of Self-Assembling Quantum Dot Arrays in III-V Semiconductor Structures. Superlattices and Microstructures **15**, 15–21 (1994)
53. P. Pfeffer, W. Zawadzki, Conduction electrons in GaAs: Five-level $\mathbf{k}\cdot\mathbf{p}$ theory and polaron effects. Phys. Rev. B **41**(3), 1561–1576 (1990)
54. P. Pfeffer, W. Zawadzki, Five-level $\mathbf{k}\cdot\mathbf{p}$ model for the conduction and valence bands of gaas and inp. Phys. Rev. B **53**(19), 12,813–12,828 (1996)
55. C.R. Pidgeon, R.N. Brown, Interband magneto-absorption and Faraday rotation in InSb. Phys. Rev. **146**, 575–583 (1966)
56. C. Pryor, Eight-band calculations of strained InAs/GaAs quantum dots compared with one-, four-, and six-band approximations. Phys. Rev. B **57**, 7190–7195 (1998)
57. C. Pryor, J. Kim, L.W. Wang, A.J. Williamson, A. Zunger, Comparison of two methods for describing the strain profiles in quantum dots. J. Appl. Phys. **83**, 2548–2554 (1998)
58. A. Puzder, A.J. Williamson, J.C. Grossman, G. Galli, Computational studies of the optical emission of silicon nanocrystals. J. Am. Chem. Soc. **125**, 2786–2791 (2003)
59. S.B. Radhia, K. Boujdaria, S. Ridene, H. Bouchriha, G. Fishman, Band structures of GaAs, InAs, and Ge: A 24-$\mathbf{k}\cdot\mathbf{p}$ model. J. Appl. Phys. **94**(9), 5726–5731 (2003)
60. S.B. Radhia, S. Ridene, K. Boujdaria, H. Bouchriha, G. Fishman, Band structures of Ge and InAs: A 20 $\mathbf{k}\cdot\mathbf{p}$ model. J. Appl. Phys. **92**(8), 4422–4430 (2002)
61. J.P. Reithmaier, G. Sek, A. Loffler, C. Hofmann, S. Kuhn, S. Reitzenstein, L.V. Keldysh, V.D. Kulakovskii, T.L. Reinecke, A. Forchel, Strong coupling in a single quantum dot-semiconductor microcavity. Nature (London) **432**, 197–200 (2004)
62. S. Richard, F. Aniel, G. Fishman, Energy-band structure of Ge, Si, and GaAs: A thirty-band $\mathbf{k}\cdot\mathbf{p}$ method. Phys. Rev. B **70**(23), 235,204 (2004)
63. D. Rideau, M. Feraille, L. Ciampolini, M. Minondo, C. Tavernier, H. Jaouen, A. Ghetti, Strained Si, Ge, and $Si_{1-x}Ge_x$ alloys modeled with a first-principles-optimized full-zone $\mathbf{k}\cdot\mathbf{p}$ method. Phys. Rev. B **74**(19), 195–208 (2006)
64. U. Rössler, Nonparabolicity and warping in the conduction band of GaAs. Solid State Commun. **49**(10), 943–947 (1984)
65. U. Rössler, J. Kainz, Microscopic interface asymmetry and spin-splitting of electron subbands in semiconductor quantum structures. Solid State Commun. **121**(6-7), 313–316 (2002)
66. M. Roy, P.A. Maksym, Efficient method for calculating electronic states in self-assembled quantum dots. Phys. Rev. B **68**, 235,308 (2003)
67. K.A. Sablon, J.W. Little, V. Mitin, A. Sergeev, N. Vagidov, K. Reinhardt, Strong enhancement of solar cell efficiency due to quantum dots with built-in charge. Nano Letters **11**(6), 2311–2317 (2011)
68. I. Saïdi, S.B. Radhia, K. Boujdaria, Band structures of gaas, inas, and inp: A 34 $\mathbf{k}\cdot\mathbf{p}$ model. J. Appl. Phys. **104**(2), 023706 (2008)
69. Saito, T., Schulman, J.N., Arakawa, Y.: Strain-energy distribution and electronic structure of InAs pyramidal quantum dots with uncovered surfaces: Tight-binding analysis. Phys. Rev. B **57**, 13,016–13,019 (1998)
70. R. Santoprete, B. Koiller, R.B. Capaz, P. Kratzer, Q.K.K. Liu, M. Scheffler, Tight-binding study of the influence of the strain on the electronic properties of InAs/GaAs quantum dots. Phys. Rev. B **68**, 235,311 (2003)

71. C. Santori, M. Pelton, G.S. Solomon, Y. Dale, Y. Yamamoto, Triggered single photons from a quantum dot. Phys. Rev. Lett. **86**, 1502–1505 (2001)
72. R.D. Schaller, V.I. Klimov, High Efficiency Carrier Multiplication in PbSe Nanocrystals: Implications for Solar Energy Conversion. Phys. Rev. Lett. **92**, 186,601 (2004)
73. W. Sheng, S.J. Cheng, P. Hawrylak, Multiband theory of multi-exciton complexes in self-assembled quantum dots. Phys. Rev. B **71**, 035,316 (2005)
74. R.M. Stevenson, R.J. Young, P. Atkinson, K. Cooper, D.A. Ritchie, A.J. Shields, A semiconductor source of triggered entangled photon pairs. Nature (London) **439**, 179–182 (2006)
75. O. Stier, Electronic and optical properties of quantum dots and wires. Wissenschaft & Technik Verlag, Berlin (2000)
76. O. Stier, M. Grundmann, D. Bimberg, Electronic and optical properties of strained quantum dots modeled by 8-band $k \cdot p$ theory. Phys. Rev. B **59**, 5688–5701 (1999)
77. M. Tadić, F.M. Peeters, K.L. Janssens, Effect of isotropic versus anisotropic elasticity on the electronic structure of cylindrical InP/$In_{0.49}Ga_{0.51}P$ self-assembled quantum dots. Phys. Rev. B **65**, 165,333 (2002)
78. M. Tadić, F.M. Peeters, K.L. Janssens, M. Korkusiński, P. Hawrylak, Strain and band edges in single and coupled cylindrical InAs/GaAs and InP/InGaP self-assembled quantum dots. J. Appl. Phys. **92**, 5819–5829 (2002)
79. S. Tomić, Electronic structure of $In_yGa_{1-y}As_{1-x}N_x$/GaAs(N) quantum dots by ten-band $\mathbf{k} \cdot \mathbf{p}$ theory. Phys. Rev. B **73**, 125,348 (2006)
80. S. Tomić, T.S. Jones, N.M. Harrison, Absorption characteristics of a quantum dot array induced intermediate band: Implications for solar cell design. Appl. Phys. Lett. **93**(26), 263105 (2008)
81. S. Tomić, A.G. Sunderland, I.J. Bush, Parallel multi-band $\mathbf{k} \cdot \mathbf{p}$ code for electronic structure of zinc blend semiconductor quantum dots. J. Mater. Chem. **16**, 1963–1972 (2006)
82. S. Tomić, Intermediate-band solar cells: Influence of band formation on dynamical processes in InAs/GaAs quantum dot arrays. Phys. Rev. B **82**, 195,321 (2010)
83. S. Tomić, N. Vukmirović, Symmetry reduction in multiband Hamiltonians for semiconductor quantum dots: The role of interfaces and higher energy bands. J. Appl. Phys. **110**(5), 053710 (2011)
84. P. Tronc, V.P. Smirnov, K.S. Zhuravlev, Symmetry of electron states and optical transitions in GaN/AlN hexagonal quantum dots. Phys. Status Solidi B **241**, 2938–2947 (2004)
85. I. Vasiliev, S. Öğüt, J.R. Chelikowsky, First-principles density-functional calculations for optical spectra of clusters and nanocrystals. Phys. Rev. B **65**(11), 115,416 (2002)
86. P. von Allmen, Conduction subbands in a GaAs/$Al_xGa_{1-x}As$ quantum well: Comparing different $\mathbf{k} \cdot \mathbf{p}$ models. Phys. Rev. B **46**(23), 15,382–15,386 (1992)
87. N. Vukmirović, Z. Ikonić, D. Indjin, P. Harrison, Symmetry-based calculation of single-particle states and intraband absorption in hexagonal GaN/AlN quantum dot superlattices. J. Phys.: Condens. Matter **18**, 6249–6262 (2006)
88. N. Vukmirović, D. Indjin, V.D. Jovanović, Z. Ikonić, P. Harrison, Symmetry of $\mathbf{k}\cdot\mathbf{p}$ Hamiltonian in pyramidal InAs/GaAs quantum dots: Application to the calculation of electronic structure. Phys. Rev. B **72**, 075,356 (2005)
89. N. Vukmirović, S. Tomić, Plane wave methodology for single quantum dot electronic structure calculations. J. Appl. Phys. **103**, 103718 (2008)
90. L.W. Wang, Large-scale local-density-approximation band gap-corrected GaAsN calculations. Appl. Phys. Lett. **78**, 1565–1567 (2001)
91. L.W. Wang, Charge-density patching method for unconventional semiconductor binary systems. Phys. Rev. Lett. **88**(25), 256,402 (2002)
92. L.W. Wang, Generating charge densities of fullerenes. Phys. Rev. B **65**, 153,410 (2002)
93. L.W. Wang, J. Kim, A. Zunger, Electronic structures of [110]-faceted self-assembled pyramidal InAs/GaAs quantum dots. Phys. Rev. B **59**(8), 5678–5687 (1999)
94. L.W. Wang, A. Zunger, Linear combination of bulk bands method for large-scale electronic structure calculations on strained nanostructures. Phys. Rev. B **59**, 15,806–15,818 (1999)
95. A.J. Williamson, A. Zunger, InAs quantum dots: Predicted electronic structure of free-standing versus GaAs-embedded structures. Phys. Rev. B **59**(24), 15,819–15,824 (1999)

96. J.B. Xia, γ-x mixing effect in GaAs/AlAs superlattices and heterojunctions, Phys. Rev. B **41**(5), 3117–3122 (1990)
97. Z. Zhou, R.A. Friesner, L. Brus, Electronic structure of 1 to 2 nm diameter silicon core/shell nanocrystals: surface chemistry, optical spectra, charge transfer, and doping. J. Am. Chem. Soc. **125**, 15,599–15,607 (2003)
98. O. Zitouni, K. Boujdaria, H. Bouchriha, Band parameters for GaAs and Si in the 24-$\mathbf{k}\cdot\mathbf{p}$ model, Semiconductor Science and Technology **20**(9), 908 (2005).
99. A. Zrenner, E. Beham, S. Stufler, F. Findeis, M. Bichler, G. Abstreiter, Coherent properties of a two-level system based on a quantum-dot photodiode. Nature (London) **418**, 612–614 (2002)